

The X-ray binary population in M33: I. Source list and luminosity function

H.-J. Grimm¹, J. McDowell¹, A. Zezas¹, D.-W. Kim¹, G. Fabbiano¹

Harvard-Smithsonian Center for Astrophysics, 60 Garden Street, Cambridge, MA 02138

ABSTRACT

In this paper we present the source list for 3 *Chandra* observations of the Local Group galaxy M33. The observations are centered on the nucleus and on the star forming region NGC 604. We detect a total of 261 sources in an area of ~ 0.2 square degree down to a flux limit of 3×10^{-16} erg s $^{-1}$ cm $^{-2}$ which corresponds to a luminosity of $\sim 2 \times 10^{34}$ erg s $^{-1}$ at a distance of 840 kpc. From the source list we construct the luminosity functions of sources observed in M33. Taking into account background contamination the luminosity functions are consistent with those of other star forming galaxies. In addition, the combination of X-ray color analysis and the existence of “blue” optical counterparts strongly indicate that the X-ray point source population in M33 consists of young objects. Above 3×10^{35} erg s $^{-1}$ there are few X-ray sources in the locus of the X-ray hardness ratio diagram that is generally populated by LMXBs.

Subject headings: X-rays: binaries — galaxies: Local Group — galaxies: individual (M33)

1. Introduction

M33 is a late-type spiral galaxy, type Sc II-III, and the third largest galaxy in the Local Group. In the Local Group it occupies a unique place since morphologically it is of intermediate type between the large early-type spiral galaxies (Milky Way and M31) and the numerous irregular galaxies. In contrast to M31 and the Milky Way, M33 does not have a stellar bulge, and also does not contain a super-massive black hole at the center (Gebhardt et al. 2001). Other galaxies of this type cannot be investigated with the same depth even with *Chandra*: at a distance of 840 kpc (Freedman et al. 1991) M33 is the second nearest spiral galaxy; it spans roughly 73×45 arcminutes on the sky; the line-of-sight absorption column density is small, $N_H \sim 6 \times 10^{20}$ cm $^{-2}$. M33 is more actively star forming (SFR \sim

¹obtained from the colden tool (<http://cxc.harvard.edu/toolkit/colden.jsp>) based on NRAO data compiled by Dickey & Lockman (1990)

$0.3\text{--}0.7 M_{\odot} \text{ yr}^{-1}$) than either the Milky Way or M31 (Hippelein et al. 2003), particularly compared to its much smaller mass. This star formation activity is visible in a number of large HII regions in the disk of M33.

As a large nearby galaxy, M33 has been observed with a number of X-ray satellites. The Einstein observatory detected 17 point sources (Trinchieri et al. 1988), among them a clear eclipsing binary (M33 X-7) (Peres et al. 1989). Markert & Rallis (1983) established the existence of an X-ray binary population based on X-ray variability and noted the association of the X-ray sources with young stellar populations. ROSAT observations led to the detection of a total 184 fainter sources coincident with Population I markers; a number of these X-ray sources are identified with SNRs (Long et al. 1996; Haberl & Pietsch 2001). BeppoSAX spectroscopy showed that the spectra of the brighter X-ray sources in M33 are consistent with X-ray binaries, and that up to 5 sources are variable (Parmar et al. 2001).

M33’s proximity, angular size, and low line-of-sight column density provide unique advantages for the study of the X-ray population of this late type spiral galaxy: 1) The same amount of detail is achievable in M33 as in M31 ($1'' = 4.1 \text{ pc}$). 2) The smaller angular size of M33 allows the observation of a larger fraction of the galaxy in a single exposure, unlike M31 or LMC/SMC. 3) The low line-of-sight N_H and the proximity of M33 allow the study of a luminosity range (few $10^{34} - 10^{38} \text{ erg s}^{-1}$) unaccessible in more distant galaxies. Sources in this luminosity range are more difficult to survey in both the Milky Way and M31 because of their larger angular sizes requiring very long observing times. Moreover, in the Milky Way distance uncertainties for individual sources, and partly high N_H make this type of study more uncertain. 4) The higher star formation rate of M33 results in a different population of X-ray sources compared to those in Milky Way and M31. 5) Its proximity combined with the positional accuracy and sensitivity of *Chandra* allows a detailed comparison of the X-ray sources with cataloged sources at other wavelengths. This is crucial to understand the X-ray source population in detail and to gain a complete picture of the X-ray binary population.

In this paper we present the source list, luminosities, X-ray luminosity functions, and identifications of X-ray point sources in M33. An accompanying paper will investigate the detailed properties and X-ray spectra of the point source population.

2. *Chandra* data and Analysis

For this study we used three of the *Chandra* observations of M33 (Table 1). A short ($\sim 12 \text{ ks}$) fourth observation, ObsId 787, was disregarded. This observation was aimed at studying the nucleus and suffers from both high background and small field of view (FOV)

(~ 54 square arcmin). Due to the angular extent of M33 all active ACIS chips cover areas of M33. These include the standard ACIS-S configuration for ObsId 786, and the standard ACIS-I configuration for ObsIds 1730 and 2023. There is considerable overlap between the different observations. However, because of the decreasing resolution/sensitivity with increasing off-axis angle only the inner parts of M33 ($\sim 8\text{--}10$ arc minutes) have a significant number of detected sources in two observations, 786 and 1730.

Table 1: List of ACIS observations of M33.

ObsId	Date	Aim point	Duration [ks]	Chips	Datemode
786	2000-08-30	Nucleus	45	ACIS-I 2–3, ACIS-S 1–4	FAINT
1730	2000-07-12	Nucleus	45	ACIS-I 0–3, ACIS-S 2–3	VFAINT
2023	2001-07-06	NGC 604	90	ACIS-I 0–3, ACIS-S 2–3	FAINT

We used CIAO 3.0.1 and 3.0.2 and CALDB 2.24 and 2.25 to analyze the data. There were no changes to the ACIS data preparation software or to the source detection software or to relevant files in the CALDB between these versions. We do not correct for enhanced absorption due to the hydrocarbon accumulation on the chips. The observations do not suffer from strong background flares, but short times of higher background (3σ above the mean) have been excluded. The effective exposure times are ~ 45 ks, ~ 43 ks, and ~ 89 ks for observations 786, 1730, and 2023, respectively. We correct for time-dependent variations of the gain with the *corr_tgain* program developed by Alexey Vikhlinin².

Source detection was performed with *wavdetect* on scales of 1, 2, 4, 8, 10, 12, and 16 pixels. The full energy range, 0.3–8.0 keV, was also subdivided in a soft, 0.3–2 keV, and hard band, 2–8 keV. Source detection was done in all the three bands. The chance detection threshold was set to 10^{-6} , equivalent to 1 spurious detection per million pixels. Due to strong pile-up, these scales fail to detect the nucleus of M33 unambiguously. Moreover, the HII regions NGC 604 and IC 131, which are more extended than the scales used, were detected by visual inspection and interactive analysis. The nucleus of M33 is strongly piled up and was therefore excluded from the analysis. For details on the nuclear source refer, e.g. to Dubus et al. (2004) and La Parola et al. (2003). The source regions correspond to the 3σ ellipses output from *wavdetect*. All source regions were inspected by eye and, if necessary, adjusted for overlapping with nearby regions and to cover the whole extent of a source. Due to the partly crowded fields, particularly near the aim point, we chose background regions on each chip in a large source-free area to ensure a sufficient number of background counts.

²http://asc.harvard.edu/cont-soft/software/corr_tgain.1.0.html

This background region was used for all sources on the corresponding chip. Since M33 has no significant intrinsic diffuse emission due to hot gas, with the exception of the inner 2 arcminutes around the nucleus, the background does not vary significantly over our FOV. Therefore our approach does not introduce significant errors in the intensity of the sources. Note that for ObsId 786 most of the sources are on the back-illuminated (BI) ACIS-S3 chip, whereas the majority of sources in the other observations is on the ACIS-I chips. The source counts were computed according to:

$$C_{source} = C - \frac{A_{source}}{A_{bkg}} \cdot C_{bkg} \cdot \frac{E_{source}}{E_{bkg}} \quad (1)$$

where C_{source} is the source counts, C is the observed counts, A_x are source and background region areas of the extraction apertures, C_{bkg} is the background counts, and $E_{source,bkg}$ are the exposures for the source and background areas. For sources that are not detected in one of the energy bands we compute upper limits on the number of source counts following the approach of Kraft et al. (1991). A few of these sources show non-zero lower limits which indicates the presence of a source. In these cases we used the most probable value for the source counts obtained with the method of Kraft et al. (1991). These sources are marked in Table 3.

In order to obtain proper positional uncertainties for our sources, which are important for identifications with objects at other wavelengths, we use the formula of Kim et al. (2004a). This formula assumes that variations in the absolute astrometric accuracy from observation to observation are small and therefore that the uncertainties depend only on count rate and off-axis angle. The positional uncertainty is given as a function of off-axis angle in the high and low count regimes. We use 100 counts to discriminate between low and high count sources. The density of point sources is small enough that sources are identified unambiguously, with the possible exception of the nucleus and the HII region NGC 604. These two cases, however, are problematic only in terms of the background they provide for other sources. In the cases where a source is observed in two or three observations, we take as the positional uncertainty the smallest value of the available observations.

To derive X-ray colors we subdivided the observations into three energy bands, soft (0.3–1.0 keV), medium (1.0–2.1 keV), and hard (2.1–8.0 keV) and measured the number of counts within the source aperture in each band. For count extraction we use the source regions in the total band from 0.3–8.0 keV. Since very faint sources, i.e. sources with less than 20 counts in the total band, are not used in the color analysis, this choice does not introduce a significant error in the extracted counts. Of the 288 sources detected in the whole band in all observations, 99 sources have less than 20 counts. Most of the sources are too faint to be investigated for spectral variability. Spectral variability of brighter sources for which spectra can be extracted will be discussed in a separate paper.

3. Point source detections

The number of sources detected with *wavdetect* in the different energy bands is given in Table 2. Note that because of the overlapping fields of view some of the sources appear in more than one observation. Also some sources are detected only in one of the three energy bands. The combined number of individual sources from all observations is 261. Among these sources 25 are detected only in the soft (0.3–2.0 keV) band and 16 only in the hard (2.0–8.0 keV) band. These hard sources have either intrinsically hard spectra or are attenuated by the ISM within M33, since the Galactic absorption towards M33 is relatively small. Fig.1 shows a DSS image of M33 overlayed with the source regions and the detector outline for the three observations.

The source list, including position, counts, and fluxes is presented in Table 3 in the Appendix: Column (1) gives the *Chandra* source name, column (2) the sky position, column (3) the positional uncertainty, columns (4), (5), and (6) the number of counts in the total, soft, and hard band for the three observations, columns (7), (8), and (9) the flux in the total, soft, and hard band for the three observations with 1σ errors. The errors given on the counts are computed using the Gehrels approximation, $\sigma = 1 + \sqrt{N + 0.75}$ (Gehrels 1986). 99% upper limits on the counts were calculated in one of two ways: 1) Because observations 1730 and 786 have the same aim point the extent of sources is comparable between these observations; thus if a source was detected in observations 1730 or 786 in another energy band, this source region was used to compute the upper limits for observations 1730 and/or 786. 2) If the source was not detected in either of these observations, upper limits were calculated from counts in a 2 arc second region around the source position.

Table 2: Number of sources detected in different energy bands and observations. Note that due to overlapping observations some of the sources appear in more than one observation. Their number for each band is given in parentheses.

ObsId	Energy band [keV]			Total No. of sources
	0.3 – 2.0	2.0 – 8.0	0.3 – 8.0	
786	79 (53)	47 (32)	96 (60)	121
1730	68 (37)	48 (30)	84 (47)	98
2023	99 (30)	68 (21)	112 (33)	129

The observation time of ObsId 2023 is twice as long as in the other two observations. This explains the larger number of sources compared to observation 1730 which uses the same instrumental configuration. The similar number of source detections in 786 and 2023 is both due to the use in 786 of the two back-illuminated (BI) chips S3 and S5 that have a higher sensitivity at low energies than the front-illuminated (FI) chips, and to the aim

at the center of M33 where the source density might be higher. Because of the different exposure times, upper limits for non-detections in the 2023 observation are smaller than in the other observations. Moreover, the $\sim 100\%$ completeness of this observation reaches down to $\sim 2 - 3 \times 10^{-15}$ erg s $^{-1}$ cm $^{-2}$ compared to $\sim 6 - 7 \times 10^{-15}$ erg s $^{-1}$ cm $^{-2}$ for both other observations. The completeness estimate is derived from simulations for correcting the luminosity function according to Kim & Fabbiano (2003). The correction is based on simulations of the detection probability of point sources with a range of flux values for various off-axis angles from the aimpoint. The simulations are performed with the MARX simulator³. The effects taken into account in the simulations are the decreasing sensitivity with increasing off-axis angle, diffuse background (not important here), uneven sky coverage of the S3 chip and telescope vignetting as described in the exposure maps.

For sources with more than 80 counts we extracted radial profiles of the source counts and fitted them with a Gaussian plus background. We compared the full-width half maximum (FWHM) of the Gaussian with a Gaussian fit of the point-spread function. For the 59 sources with sufficient counts we find no evidence of extended emission.

Given the large area covered by the observations, we expect to have serious contamination by background AGN, in particular at fainter luminosities. Based on data from the Chandra Deep Field–North (CDF-N) (Alexander et al. 2003) we estimate that of order 50% of the sources detected with luminosities in the range $10^{34} \leq L_X \leq 5 \times 10^{35}$ erg s $^{-1}$ are background AGN. Pietsch et al. (2004) arrive at a comparable fraction for the XMM field, which is roughly four times larger than the area covered by *Chandra*. The XMM-Newton observation is on average less deep than the *Chandra* observations. Cosmic variance may change the number of background AGN slightly but based on data from the CHAMP survey cosmic variance does not appear to be a strong effect (Kim et al. 2004b). A more detailed estimate of the actual number of background objects requires a more detailed knowledge of the source properties. Above $L_X \geq 5 \times 10^{35}$ contamination of the luminosity function is small because the AGN Log(N)–Log(S) is much steeper than the luminosity function of galactic X-ray sources.

4. Point source colors

Hardness–ratio diagrams are a straightforward way to classify sources in general, especially for sources that do not have sufficient number of counts to allow spectral fitting (Kim et al. 1992; Prestwich et al. 2003).

³<http://space.mit.edu/ASC/MARX/>

From the counts extracted from the three different bands mentioned in Sec. 2 we construct two colors, a soft color and a hard color. The soft color is defined as

$$HR1 = \frac{M - S}{S + M + H} \quad (2)$$

and the hard color as

$$HR2 = \frac{H - M}{S + M + H}, \quad (3)$$

where S , M , and H are the counts in a soft (0.3–1.0 keV), medium (1.0–2.1 keV), and hard (2.1–8.0 keV) energy band, respectively. The energy bands were selected to achieve an optimal separation between soft/thermal and hard/power law components (Prestwich, private comm.). The results for the different observations are shown in Fig.2. Following Prestwich et al. (2003) we consider here only sources with more than 20 detected counts in the full band to somewhat reduce statistical errors on the colors. The errors on the counts are computed with Gehrels approximation (Gehrels 1986); errors on the colors are computed using standard error propagation. Note that for small number of counts the errors must not be regarded as Gaussian 68% limits. We disregard sources that have upper limits in any of the bands. Typical net counts for the sources are in the range from 30–50 counts. The detected number of counts is dependent on the response of the CCD. This difference is expected to be largest between FI and BI chips. Therefore we plot the hardness ratios in separate panels. The model tracks in Fig.2 were computed separately for the BI (ObsId 786) and FI chips (ObsIds 1730 & 2023). The strong similarity of the tracks indicates that differences in the CCD response between our observations do not have a strong effect on the colors, at least for sources with more than ~ 20 counts.

In Sec. 7 we will use optical identification together with colors to investigate the color relations of different source types in more detail.

5. Luminosity function

Since the *Chandra* observations have different exposure times and cover somewhat different areas, we present here the luminosity functions for each observation separately. Fig.3 shows the observed luminosity functions. The black lines show the sources detected in the whole band (0.3–8.0 keV), the dotted line sources detected in the soft band (0.3–2.0 keV), and the dashed line sources detected in the hard band (2.0–8.0 keV).

The count to luminosity conversion was established based on the fit of source spectra with more than 100 counts with XSPEC 11.3.0. The typical spectrum for the fainter sources in this range, ~ 100 –200 counts, is an absorbed power law with Galactic absorption, $6 \times$

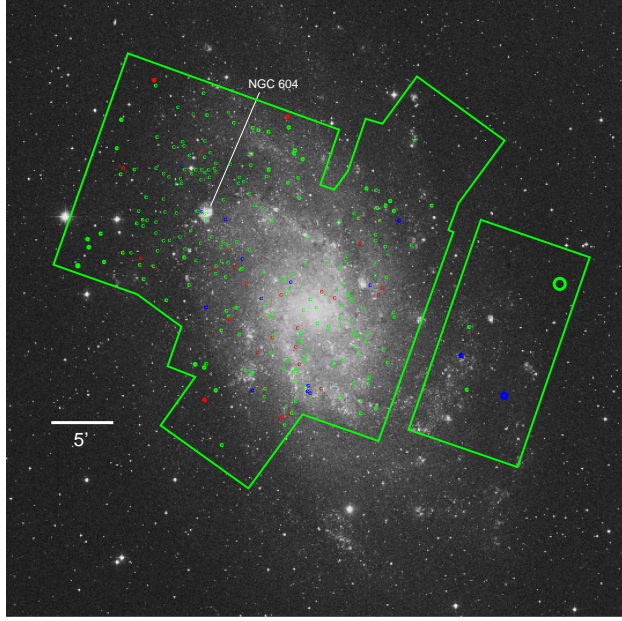


Fig. 1.— DSS image of M33 overlaid with source regions and the envelope of the *Chandra* field of view. North is up, and east is left.

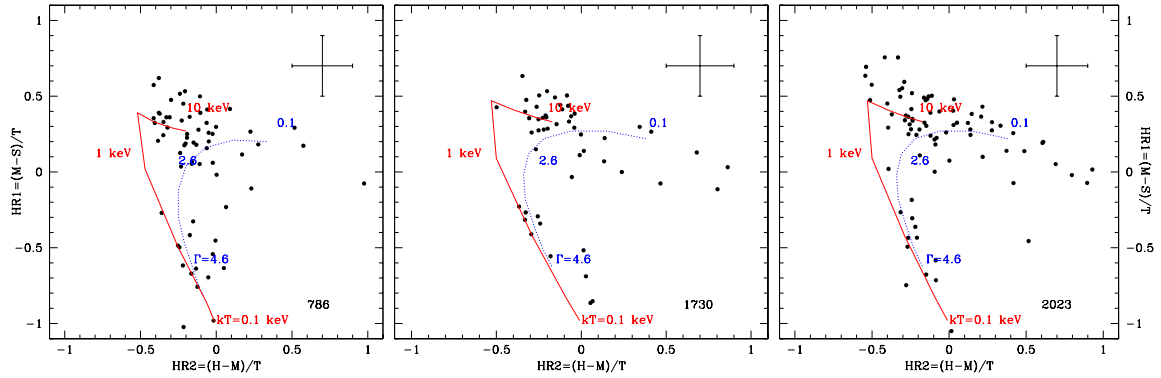


Fig. 2.— Hardness ratio diagrams for the three *Chandra* observations. The solid line is a model path for a black body spectrum, the dotted line a model for a power law, both with Galactic absorption and taking into account different responses of the main CCDs in the observations. The CCD response is not a strong effect. Increasing absorption moves the lines to the upper left corner. The cross represents a typical error bar for a source with 35–40 counts.

10^{20} cm $^{-2}$, and a photon index of ~ 2.0 . This spectrum roughly describes an X-ray binary spectrum, the sources of particular interest. These values are assumed for fainter sources for the conversion from counts to flux. The values quoted in the following for sources with more than 100 counts are the fitted observed values. As a rule of thumb 100 counts correspond to a luminosity of $1-2 \times 10^{36}$ erg s $^{-1}$. The spectra of the brighter sources are roughly consistent with such a spectrum. The details of spectral fitting will be discussed in a separate paper.

In Fig.4 we present the luminosity functions in the full band after correcting for incompleteness by applying the procedure outlined in Kim & Fabbiano (2003). A comparison with Fig.3 shows the importance of this correction for obtaining the actual shape of the luminosity function.

A Kolmogorov-Smirnov test shows that the luminosity functions have a probability higher than 95% to be drawn from the same distribution. The slopes of the luminosity functions are relatively steep for an actively star forming galaxy. A Maximum-Likelihood fit gives slopes for cumulative luminosity function for the observations 786, 1730, and 2023 of 0.78 ± 0.17 , 0.76 ± 0.14 , and 0.74 ± 0.13 , respectively. The effect of interloper contamination on these slopes is discussed in Sec. 7.2.

6. Counterparts

In order to gain more information about the nature of the X-ray sources we cross-correlate our sources with a number of different catalogs available for M33. Given the proximity of M33 and the resulting good resolution, there is a large amount of data in many wavebands. We used the SIMBAD database to find catalogs pertaining to M33, and we also cross-correlated the positions of individual *Chandra* sources against the whole SIMBAD database. We discuss below the results of these comparisons with X-ray catalogs and multi-wavelength databases separately.

We cross-correlated our source list with the following catalogs: The XMM-Newton survey of M33 (Pietsch et al. 2004), the ROSAT source catalog (Haberl & Pietsch 2001), the catalog of SNR by Gordon et al. (1999), HII regions from Hodge et al. (1999), giant molecular clouds from Engargiola et al. (2003), globular clusters from Mochejska et al. (1998), star clusters from Chandar et al. (1999) and Chandar et al. (2001), blue and red supergiants from Ivanov et al. (1993), red supergiants from Massey (1998), Wolf-Rayet stars from Massey & Johnson (1998), UV bright stars from Massey et al. (1996), hot stars from Massey et al. (1995), OB associations from Regan & Wilson (1993), planetary nebulae from Magrini et al. (2001), H α emitters from Calzetti et al. (1995), and the DIRECT star catalog from Macri

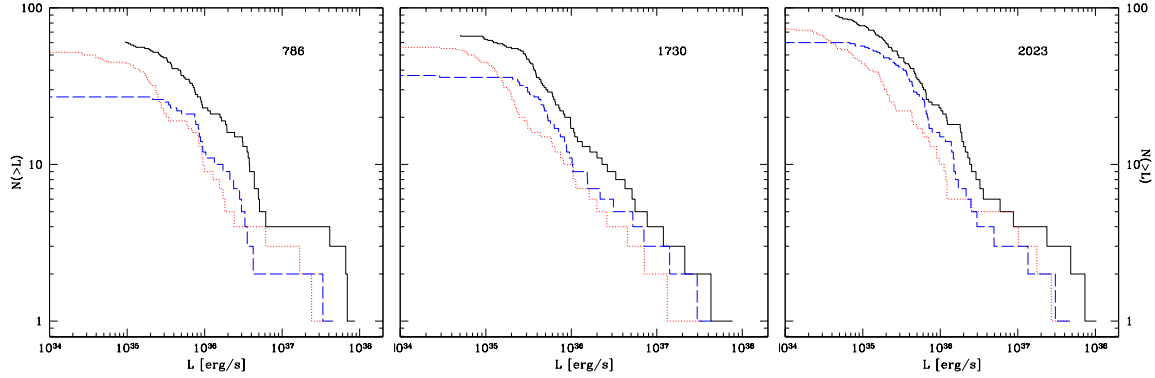


Fig. 3.— Luminosity functions for the three *Chandra* observations. The black lines show the sources detected in the whole band (0.3–8.0 keV), the dotted line sources detected in the soft band (0.3–2.0 keV), and the dashed line sources detected in the hard band (2.0–8.0 keV).

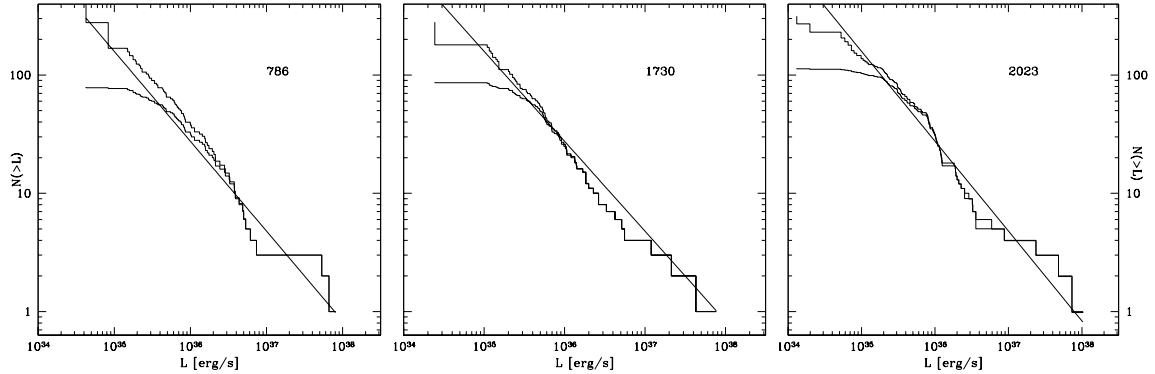


Fig. 4.— Corrected and uncorrected luminosity functions for the three *Chandra* observations. The histograms show the sources detected in the whole band (0.3–8.0 keV). The solid line (the same in each panel) is the best fit power law for the luminosity function of ObsId 1730. The scale is the same in all panels.

et al. (2001).

The cross-correlation is done using the uncertainty of the *Chandra* source position, computed according to Kim et al. (2004a). In addition the source uncertainty of catalog positions was quadratically added to the *Chandra* positional uncertainty. If no such number is available in the catalogs, an uncertainty of 1 arcsec was added. If there are more than one source in the error circle we make no further assumption about the likelihood of any of the sources *within* the error circle being a real counterpart of the X-ray source.

6.1. X-ray counterparts

M33 has been observed with various X-ray missions, most notably ROSAT and recently XMM-Newton. Haberl & Pietsch (2001) have analyzed all available ROSAT observations and extracted a total of 184 sources. The ROSAT observations cover a much larger area of M33 than our *Chandra* observations. Also note that the ROSAT (0.1–2.4 keV) and *Chandra* energy bands (0.3–8.0 keV) are different. Only 115 ROSAT sources are in the field of view of the *Chandra* observations. Of these 115 sources, we detect 50 with *Chandra*: Twelve of these are supernova remnants (SNR) as classified by Haberl & Pietsch (2001), three supersoft sources (SSS), two X-ray binaries (XRB), including M33 X-7 (Peres et al. 1989) the first such identification, and two foreground stars. Of the ROSAT detections 20 sources are far off-axis ($\gtrsim 8$ arcmin) in any *Chandra* observation, and 22 are observable in only one observation. Table 5 in the Appendix contains the matches of *Chandra* and ROSAT sources. Column (1) is the *Chandra* source name, column (2) the *Chandra* positional uncertainty, column (3) RA and Dec of the ROSAT source, column(4) the ROSAT positional uncertainty, column (5) the ROSAT name, column (6) the HRI flux and the corresponding 1σ error. The typical astrometric error for the ROSAT sources is ~ 5 arcsec with a long tail to larger errors; 32 sources have positional uncertainties larger than or equal to 20 arcsec.

The XMM-Newton observations of M33 were of relatively shallow exposure, lasting generally between ~ 10 –15 ks (Pietsch et al. 2004). Their detection limit of $\sim 1.4 \times 10^{-15}$ erg s $^{-1}$ cm $^{-2}$ for a power law with $\Gamma = 1.7$ and $N_H = 6 \times 10^{20}$ cm $^{-2}$ compares to our $\sim 3 \times 10^{-16}$ erg s $^{-1}$ cm $^{-2}$. Like the ROSAT observations, this XMM survey also covers a larger area than *Chandra*. Of the 408 sources detected by XMM, 184 are in the *Chandra* fields of view. Of these 184 sources 102 are detected with *Chandra*, including 13 SNRs, two SSSs, one XRB, three foreground stars, four background AGN, and 35 hard sources as defined by Pietsch et al. (2004). Table 6 in the Appendix contains the *Chandra* and XMM matches. Column (1) is the *Chandra* source name, column (2) the *Chandra* positional uncertainty, column (3) RA and Dec of the XMM source position, column (4) XMM energy flux and 1σ error, column

(5) the XMM X-ray identification.

6.2. Other wavebands

The correlation with the radio data from Gordon et al. (1999) yields 24 matches, 14 of which are SNRs or candidate SNRs based on their radio spectral slope. One SNR matches two *Chandra* sources. Five SNRs are associated with HII regions. Nine matches are foreground/background objects. The radius assigned for sources of the whole catalog is 3 arcsec. The optical radius of the SNRs is on average 4.5 arcsec. Taking the actual optical radius to match *Chandra* sources with selected SNRs in Table 4 of Gordon et al. (1999) does not change the result for the SNR matches. We expect less than three chance coincidences at 95% for the whole catalog and less than two for the selected SNRs.

There is one association with a globular cluster in M33 from the sample of Mochejska et al. (1998). The assumed radius of the clusters is 2 arcsec. The number of expected chance coincidences is less than 1. This source is also the only match with the samples of Chandar et al. (1999) and Chandar et al. (2001) (also 2 arcsec radius). This source does not match any other catalog, however its location in a globular cluster suggests that it is either a bright CV or a low-mass X-ray binary (LMXB).

There are nine matches with blue stars in M33 from the sample of Ivanov et al. (1993) for seven *Chandra* sources; two *Chandra* sources match two blue stars each. The accuracy for the blue star positions is 1.5 arcsec (Ivanov et al. 1993). None of the red stars in the Ivanov et al. (1993) sample matches any *Chandra* source. Due to the highly clustered nature of the blue supergiants it is not straightforward to calculate the probability of chance coincidences. However, it is possible that the majority of matches are not real.

Due to the large number of objects, roughly 60000, a matching with DIRECT sources yields ambiguous results. The limiting magnitude of the catalog is 23.6 in V. For off-axis angle sources (~ 4 arcmin) where the *Chandra* beam is large, there are numerous associations. But for *Chandra* sources closer to the aim point, and a correspondingly smaller error radius (≤ 1 arcsec), there are also 43 unique counterparts. However, because of the very high density of DIRECT objects, most of them are likely chance coincidences.

Similarly to the DIRECT sources, OB stars from Regan & Wilson (1993) have a high density and give multiple matches. In total there 14 matches with nine *Chandra* sources, six of which are unique matches. The positional accuracy of the OB stars is within 2 arcsec (Regan & Wilson 1993). The high source density and overlapping source regions indicate that the majority of matches are chance coincidences.

The HII region sample of Hodge et al. (1999) gives three matches. As radius for the HII regions we use the optical radius if given, otherwise we use 1 arcsec. Despite the small radius, the number of expected chance coincidences is still three because of the large number of HII regions (~ 1200).

The UV stars in M33 in the sample of Massey et al. (1996) yield six matches (uncertainty 1.4 arcsec, 2 chance coincidences expected). One of the sources is identified with a B1 supergiant, another with a LBV candidate, and another one with an HII region. One of the *Chandra* sources is also the only match with the Wolf-Rayet star sample of Massey & Johnson (1998). There is also only one match with the catalog of hot stars of Massey et al. (1995). For the two later catalogs an uncertainty of 1 arcsec was assumed and 1 chance coincidence is expected in each.

7. Discussion

7.1. Source types

Due to the comparable number of expected background sources and sources associated with M33 in our dataset it is important to distinguish the different source types. Only by identifying the X-ray sources is it possible to learn more about the true source population of M33. As a first step we compare X-ray colors with the expected location of different source types in the hardness–ratio diagram. Again sources with upper limits in any band are disregarded. In Fig.5 we show different source types, derived from identifications in other wavelengths: filled circles show supernova remnants; stars are background and foreground objects; open squares are objects with a “blue” counterpart, blue meaning either an H_{α} , UV, U or B band counterpart detected in M33. As can be easily seen from the picture, SNRs do populate the expected locus in the hardness–ratio diagram based on the prescription of Prestwich et al. (2003). There is only one exception of an SNR from the Gordon catalog which has a harder X-ray spectrum than expected of a thermal SNR, and might either be a plerionic SNR or an SNR harboring an X-ray binary.

Comparing the X-ray hardness ratio diagram with the regions Prestwich et al. (2003) identified with certain source types in Fig.5 shows that the region that covers LMXBs, around (-0.3,0) in HR2–HR1, is only sparsely populated whereas all other regions are well populated with sources. The distribution of points in the color diagram, and in particular the avoidance of the LMXB locus is reinforced if we consider Fig. 2 which contains both identified and unidentified sources. AGN and pulsar-like X-ray binaries are not distinct in the hardness ratio diagram, both being consistent with hard and/or possibly absorbed sources. Note that

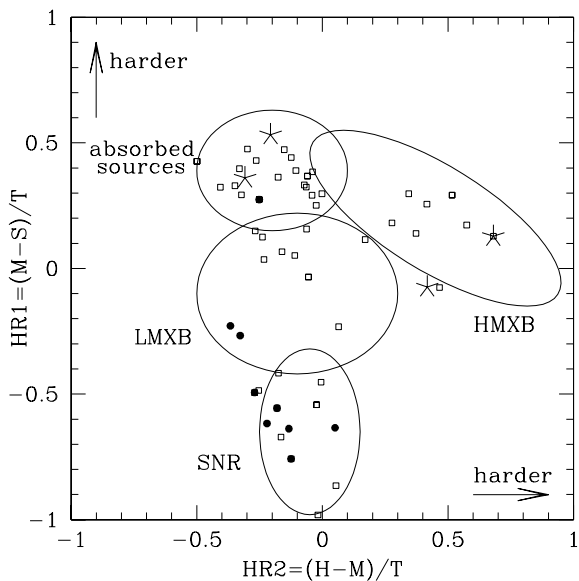


Fig. 5.— Hardness-ratio diagram of sources with identifications. Filled circles—SNR, stars—background/foreground objects, open squares—"blue" counterparts. The elliptical areas indicate the expected location of various source types. The areas are taken from Prestwich et al. (2003). Only sources with no upper limits in any flux band are shown. For more details see Sec. 7.1.

very strongly absorbed sources ($N_H \geq 10^{22} \text{ cm}^{-2}$) would not be plotted because they would not be detected in the soft band if they were not very bright. This implies that LMXBs do not contribute significantly to the X-ray source population in M33. This is consistent with the estimate of its stellar mass and star formation rate which suggests a prevalent young stellar population.

Although the regions shown in Fig.5 do not represent a quantitative expectation value for different source locations, we can nevertheless quantify our expectations for the number of HMXBs and LMXBs from the universal luminosity functions for HMXBs (Grimm et al. 2003) and LMXBs (Gilfanov 2004). We take the star formation rate of M33 to be $\sim 0.3 \text{ M}_\odot \text{ yr}^{-1}$ (Hippelein et al. 2003), and the K band magnitude to be $m_K = 4.1$ (Jarrett et al. 2003). Using eq. (22) of Grimm et al. (2003) and eq. (21) with the normalization for late-type galaxies of Gilfanov (2004), we expect to observe $\sim 6 - 7$ HMXBs and ~ 3 LMXBs above $10^{37} \text{ erg s}^{-1}$. At $10^{37} \text{ erg s}^{-1}$ we expect no strong contamination by background sources. These numbers are in good agreement with the observed number of 6 sources above $10^{37} \text{ erg s}^{-1}$. Although the *Chandra* observations do not cover M33 in its entirety they cover more than 80% of M33. The expected total luminosity is $\sim 3.5 \times 10^{38} \text{ erg s}^{-1}$ for HMXBs and $\sim 10^{38} \text{ erg s}^{-1}$ for LMXBs. These values agree very well with the observed total X-ray luminosity of point sources (excluding the nucleus) of $\sim 3 - 4 \times 10^{38} \text{ erg s}^{-1}$. Using the formulae of Colbert et al. (2004) for the relation of total X-ray luminosities with K-band luminosity, FIR+UV luminosities, as well as with stellar mass and SFR give basically identical results. An exception is the X-ray–stellar mass relation, which predicts an LMXB X-ray luminosity of $\sim 1.2 \times 10^{39} \text{ erg s}^{-1}$, an order of magnitude larger than predicted by other relations, and 3–4 times larger than the observed luminosity.

7.2. Luminosity function

Based on spectrophotometry and comparison with theoretical SEDs M33 is expected to be dominated by a young stellar population (Li et al. 2004), in agreement with the source colors as discussed in Sec. 7.1. Therefore most X-ray sources in M33 should be high-mass X-ray binaries (HMXB). We would then expect the luminosity function of the M33 sources to be similar to the luminosity function of HMXBs in the Milky Way. Fig.6 shows the corrected luminosity functions of M33 and the luminosity functions of HMXBs in the Milky Way (thick solid histogram) and in the SMC (dotted histogram). The luminosity functions differ slightly in shape but have a similar slope within the errors. The SMC luminosity function seems to be somewhat flatter but there is a large contribution from the four brightest sources in the SMC. On the other hand the M33 luminosity functions obtained from Maximum-Likelihood

fits are steeper ($\sim 0.76 \pm 0.14$) than the Milky Way HMXB luminosity function (0.64 ± 0.15) though still consistent within the errors.

These values for the slope of the M33 luminosity functions lie in between what is found for star forming galaxies, $\alpha \sim 0.5 - 0.6$ (Kilgard et al. 2005), and elliptical galaxies, $\alpha \sim 1$ (Kim & Fabbiano 2004). The reason for the steep luminosity function is most likely the expected large number of background objects ($\sim 50\%$) which will steepen the luminosity function due to their steep number-flux relation (Alexander et al. 2003). A significant contribution of LMXBs is unlikely since the stellar mass of M33 is roughly one tenth of the Milky Way and therefore the number of LMXBs are expected to be similarly small (~ 10 above 10^{36} erg s $^{-1}$ in all of M33). Moreover, at low luminosities ($L_X < 10^{37}$ erg s $^{-1}$) the LMXB luminosity function flattens as well (Grimm et al. 2002; Kong et al. 2002).

We compared our number-flux relation with the 2Ms CDF-N source catalog of Alexander et al. (2003) in the full band⁴. In order to compare the CDF-N data with our analysis of M33 we take into account different assumptions about spectral shape, different fields of view and different column densities. Alexander et al. (2003) assume a power law spectrum with a photon index of $\Gamma = 1.4$, a Galactic absorption column density of $N_H = 1.6 \times 10^{20}$ cm $^{-2}$, and compute the flux in the energy range from 0.5–8.0 keV. Converting the fluxes to our values of $\Gamma = 2$ and $N_H = 6 \times 10^{20}$ cm $^{-2}$ in the energy range from 0.3–8.0 keV results in a correction factor of ~ 0.5 for the CDF-N data. Moreover, the different fields of view used in the CDF-N analysis and our analysis (note we correct our observations individually) yields another factor of ~ 0.6 with respect to the CDF-N data for the number of sources. The first factor obviously depends only on assumptions about spectral shape and energy band used. The second factor, however, is subject to uncertainties arising from the (non-)existence of cosmic variance. This background can significantly affect the normalization of the background Log(N)–Log(S).

We find that after subtracting the corrected CDF-N number-flux relation from the M33 ones the slope flattens to $\sim 0.5 - 0.6$. Note that this is an estimate of slope, not a fit. The slopes are flatter for higher background normalizations. However the range is relatively robust for reasonable assumptions about the normalization of the background Log(N)–Log(S) arising from cosmic variance, i.e. changes in normalization of a factor of 2–3. We also compare the soft band (0.3–2.0 keV) luminosity function with ROSAT All-Sky Survey data from fields adjacent to M33. Slope and normalization of the RASS Log(N)–Log(S) are consistent with the values from the CDF-N in the overlapping flux range. The

⁴The data were obtained from Neil Brandt’s web page <http://www.astro.psu.edu/users/niel/hdf/hdf-chandra.html>

solid line in Fig.6 is an approximation to the *intrinsic* M33 luminosity function with a slope of 0.55, and a normalization fixed by the brightest sources. A more detailed study of luminosity functions and background Log(N)–Log(S) is necessary to quantify these results further.

Fig.7 shows the luminosity function of M33 overlayed with the fitted luminosity functions for different regions of M31 (Kong et al. 2003). The dashed line is the luminosity function for a region in the outer parts of M31 and has a slope of 1.1, the dash-dotted line is for a region in the disk of M31, and the dotted line is for a region including parts of the star forming ring around the bulge of M31. The solid line is again the approximation to the *intrinsic* M33 luminosity function. The dash-dotted and dotted lines, dominated by young stellar populations, resemble the luminosity functions of M33 most closely.

The similarity of the *intrinsic* slopes in M33 and the shapes of the luminosity function with HMXB luminosity functions in the Milky Way and starburst galaxies shows, that the X-ray source population in M33 is dominated by HMXBs and other young X-ray sources. It also agrees with the assumption that LMXBs do not contribute significantly to the X-ray binary population in M33.

7.3. Supernova remnants

Supernova remnants are another source type associated with young stellar populations. The X-ray luminosity distribution of 16 SNRs detected both in radio (Gordon et al. 1999) and with *Chandra* is shown in Fig.8. Due to the construction of the correction of the intensity distribution by Kim et al. (2004a) it is not possible to correct the luminosity function of a subset of sources. Therefore the SNR luminosity function is not corrected for incompleteness.

For comparison we show the luminosity function of SNRs in M33, and in the Magellanic Clouds and M31 obtained from ROSAT data in Fig.8. The data for M31 (dotted histogram) are taken from observations by Supper et al. (2001), the data on the Magellanic Clouds (dashed histogram for LMC, dot-dashed histogram for SMC) are from Sasaki et al. (2000a) and Sasaki et al. (2000b). The data are not corrected for the different energy bands of *Chandra* and ROSAT. For thermal supernova remnants most of the flux is in the soft band, so the extended *Chandra* response towards hard X-rays will not significantly change the luminosity for these sources. Also different assumptions about spectral shape do not strongly affect the luminosities in this energy range. Although numerous SNRs are known in the Milky Way, their poorly determined distances and non-uniform sampling do now allow a comprehensive comparison with the population with extragalactic SNRs.

Although there are relatively few sources, SNRs in the SMC are underluminous com-

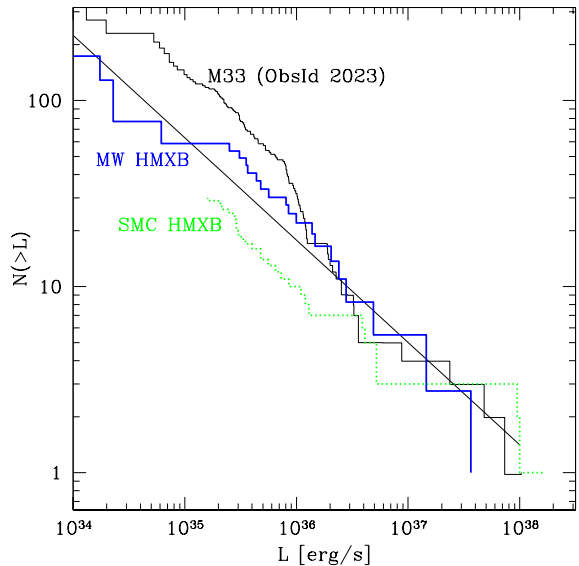


Fig. 6.— Luminosity functions of X-ray sources in M33 from ObsId 2023 (solid histograms) compared with the HMXB luminosity function of the Milky Way (thick solid histogram) (Grimm et al. 2002) and X-ray binary candidates in the SMC (thick dotted histogram) (Yokogawa et al. 2000). The solid line is a representation of the expected intrinsic luminosity function of M33 after subtraction of background AGN with a cumulative slope of 0.55. The normalization of the expected intrinsic luminosity function of M33 is defined by the high luminosity end of the luminosity function of ObsId 2023.

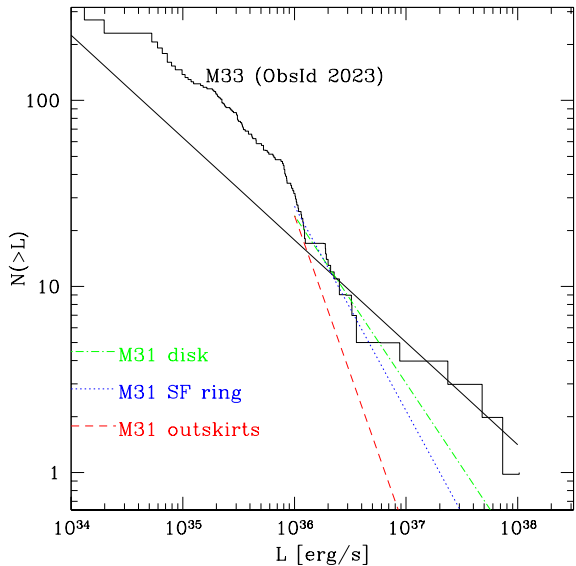


Fig. 7.— Luminosity functions of X-ray sources in M33 from ObsId 2023 compared with luminosity function fits from regions in M31 by Kong et al. (2003). The dashed line is the luminosity function (slope of 1.1) for a region in the outer parts of M31, the dash-dotted line is for a region in the disk of M31, and the dotted line is for a region including parts of the star forming ring around the bulge of M31. The solid line is a representation of the expected intrinsic luminosity function of M33 after subtraction of background AGN with a cumulative slope of 0.55 and a normalization defined by the high luminosity end of the observed luminosity function.

pared with SNRs in the other galaxies. This has been noted already by Haberl & Pietsch (2001) and the authors attribute this to higher metal abundances in the LMC. Although the luminosities in M33, M31, and the LMC are comparable, a two sample Kolmogorov-Smirnov test gives a probability of only $\sim 1\%$ for the luminosity functions of M31 and M33, and the Magellanic Clouds, to have the same underlying distribution. However, for M33 and the Magellanic Clouds the probability increases to $\sim 10\%$. And for LMC and SMC the probability increases to over 60%. Even considering the different incompleteness limits and instrumental effects (M31 – PSPC, the Magellanic Clouds – HRI) there nevertheless might be a difference in the SNR population in star forming and older galaxies. For a complete and more concise discussion of the SNRs in M33, refer to Ghavamian et al. (2005) who investigate the properties of the SNRs individually.

8. Conclusion

The sensitivity of the *Chandra* observations of M33, and the wealth of multi-wavelength data for this galaxy does allow a uniquely detailed study of the X-ray point source population.

Here we present the source list, counterparts, X-ray colors, and X-ray luminosity functions of sources in M33 observed with *Chandra*. In total 261 individual sources are detected in 3 partly overlapping observations down to a flux of 3×10^{-16} erg s $^{-1}$ cm $^{-2}$, corresponding to a luminosity of $\sim 2 \times 10^{34}$ erg s $^{-1}$ at a distance of 840 kpc. The observations are centered on the nucleus and the star forming region NGC 604. The luminosity functions of the observations are statistically consistent with each other. Because of the large area covered by the observation, ~ 0.2 square degrees, the number of background objects is large. Based on CDF-N data we conclude that around 50% of the detected sources are background objects at low luminosities ($10^{34} \leq L_X \leq 5 \times 10^{35}$ erg s $^{-1}$).

Taking into account the contribution of background AGN to the luminosity function of M33, the slope of the luminosity function, cumulative $\sim 0.5 - 0.6$, is consistent with HMXB luminosity functions in the Milky Way and the Magellanic Clouds. Color analysis of the sources shows a lack of sources at the location populated by low-mass X-ray binaries in the X-ray color-color diagram. Also cross-correlations with catalogs at other wavelengths result preferably in matches with objects associated with young stellar populations: e.g. SNRs, blue stars, HII regions. We therefore conclude that the X-ray source population in M33 is dominated by a young population, similar to other star forming galaxies. This is also in agreement with expectations based on the stellar mass and star formation rate of M33.

We also find that the shape of the luminosity function of SNRs in M33 is more similar

to the SNR luminosity functions in the Magellanic Clouds (Sasaki et al. 2000a,b) than to the SNRs in M31 (Supper et al. 2001). This might be related to abundance differences in these galaxies (Haberl & Pietsch 2001).

The spectral properties, along with temporal properties, of sources with a sufficient number of counts will be discussed in a following paper.

9. Acknowledgments

This work has been supported by NASA grant GO2-3135X. The authors want to thank Ralph Kraft for his program to compute upper limits, and Wolfgang Pietsch for providing the XMM source list before publication. We also thank the referee for constructive comments on the paper.

REFERENCES

- Alexander, D. M., Bauer, F. E., Brandt, W. N., Schneider, D. P., Hornschemeier, A. E., Vignali, C., Barger, A. J., Broos, P. S., Cowie, L. L., Garmire, G. P., Townsley, L. K., Bautz, M. W., Chartas, G., & Sargent, W. L. W. 2003, AJ, 126, 539
- Calzetti, D., Kinney, A. L., Ford, H., Doggett, J., & Long, K. S. 1995, AJ, 110, 2739
- Chandar, R., Bianchi, L., & Ford, H. C. 1999, ApJS, 122, 431
- . 2001, A&A, 366, 498
- Colbert, E. J. M., Heckman, T. M., Ptak, A. F., Strickland, D. K., & Weaver, K. A. 2004, ApJ, 602, 231
- Dickey, J. M. & Lockman, F. J. 1990, ARA&A, 28, 215
- Dubus, G., Charles, P. A., & Long, K. S. 2004, A&A, 425, 95
- Engargiola, G., Plambeck, R. L., Rosolowsky, E., & Blitz, L. 2003, ApJS, 149, 343
- Freedman, W. L., Wilson, C. D., & Madore, B. F. 1991, ApJ, 372, 455
- Gebhardt, K., Lauer, T. R., Kormendy, J., Pinkney, J., Bower, G. A., Green, R., Gull, T., Hutchings, J. B., Kaiser, M. E., Nelson, C. H., Richstone, D., & Weistropp, D. 2001, AJ, 122, 2469

- Gehrels, N. 1986, ApJ, 303, 336
- Ghavamian, P., Blair, W. P., Long, K. S., Sasaki, M., Gaetz, T. J., & Plucinsky, P. P. 2005, AJ, accepted
- Gilfanov, M. 2004, MNRAS, 349, 146
- Gordon, S. M., Duric, N., Kirshner, R. P., Goss, W. M., & Viallefond, F. 1999, ApJS, 120, 247
- Grimm, H.-J., Gilfanov, M., & Sunyaev, R. 2002, A&A, 391, 923
- . 2003, MNRAS, 339, 793
- Haberl, F. & Pietsch, W. 2001, A&A, 373, 438
- Hippelein, H., Haas, M., Tuffs, R. J., Lemke, D., Stickel, M., Klaas, U., & Völk, H. J. 2003, A&A, 407, 137
- Hodge, P. W., Balsley, J., Wyder, T. K., & Skelton, B. P. 1999, PASP, 111, 685
- Ivanov, G. R., Freedman, W. L., & Madore, B. F. 1993, ApJS, 89, 85
- Jarrett, T. H., Chester, T., Cutri, R., Schneider, S. E., & Huchra, J. P. 2003, AJ, 125, 525
- Kilgard, R. E., Cowan, J., Garcia, M. R., Kaaret, P., Krauss, M., McDowell, J., Prestwich, A., Primini, F., Stockdale, C., Trinchieri, G., Ward, M., & Zezas, A. 2005, ApJS, submitted
- Kim, D. & Fabbiano, G. 2003, ApJ, 586, 826
- Kim, D.-W., Cameron, R. A., Drake, J. J., Evans, N. R., Freeman, P., Gaetz, T. J., Ghosh, H., Green, P. J., Harnden, F. R., Karovska, M., Kashyap, V., Maksym, P. W., Ratzlaff, P. W., Schlegel, E. M., Silverman, J. D., Tananbaum, H. D., Vikhlinin, A. A., Wilkes, B. J., & Grimes, J. P. 2004a, ApJS, 150, 19
- Kim, D.-W. & Fabbiano, G. 2004, American Astronomical Society Meeting, 204,
- Kim, D.-W., Fabbiano, G., & Trinchieri, G. 1992, ApJS, 80, 645
- Kim, D.-W., Wilkes, B. J., Green, P. J., Cameron, R. A., Drake, J. J., Evans, N. R., Freeman, P., Gaetz, T. J., Ghosh, H., Harnden, F. R., Karovska, M., Kashyap, V., Maksym, P. W., Ratzlaff, P. W., Schlegel, E. M., Silverman, J. D., Tananbaum, H. D., & Vikhlinin, A. A. 2004b, ApJ, 600, 59

- Kong, A. K. H., DiStefano, R., Garcia, M. R., & Greiner, J. 2003, ApJ, 585, 298
- Kong, A. K. H., Garcia, M. R., Primini, F. A., Murray, S. S., Di Stefano, R., & McClintock, J. E. 2002, ApJ, 577, 738
- Kraft, R. P., Burrows, D. N., & Nousek, J. A. 1991, ApJ, 374, 344
- La Parola, V., Damiani, F., Fabbiano, G., & Peres, G. 2003, ApJ, 583, 758
- Li, J., Ma, J., Zhou, X., Jiang, Z., Yang, Y., & Chen, J. 2004, A&A, 420, 89
- Long, K. S., Charles, P. A., Blair, W. P., & Gordon, S. M. 1996, ApJ, 466, 750
- Macri, L. M., Stanek, K. Z., Sasselov, D. D., Krockenberger, M., & Kaluzny, J. 2001, AJ, 121, 861
- Magrini, L., Cardwell, A., Corradi, R. L. M., Mampaso, A., & Perinotto, M. 2001, A&A, 367, 498
- Markert, T. H. & Rallis, A. D. 1983, ApJ, 275, 571
- Massey, P. 1998, ApJ, 501, 153
- Massey, P., Armandroff, T. E., Pyke, R., Patel, K., & Wilson, C. D. 1995, AJ, 110, 2715
- Massey, P., Bianchi, L., Hutchings, J. B., & Stecher, T. P. 1996, ApJ, 469, 629
- Massey, P. & Johnson, O. 1998, ApJ, 505, 793
- Mochejska, B. J., Kaluzny, J., Krockenberger, M., Sasselov, D. D., & Stanek, K. Z. 1998, Acta Astronomica, 48, 455
- Parmar, A. N., Sidoli, L., Oosterbroek, T., Charles, P. A., Dubus, G., Guainazzi, M., Hakala, P., Pietsch, W., & Trinchieri, G. 2001, A&A, 368, 420
- Peres, G., Reale, F., Collura, A., & Fabbiano, G. 1989, ApJ, 336, 140
- Pietsch, W., Misanovic, Z., Haberl, F., Hatzidimitriou, D., Ehle, M., & Trinchieri, G. 2004, A&A, 426, 11
- Prestwich, A. H., Irwin, J. A., Kilgard, R. E., Krauss, M. I., Zezas, A., Primini, F., Kaaret, P., & Boroson, B. 2003, ApJ, 595, 719
- Regan, M. W. & Wilson, C. D. 1993, AJ, 105, 499

- Sasaki, M., Haberl, F., & Pietsch, W. 2000a, A&AS, 143, 391
—. 2000b, A&AS, 147, 75
- Supper, R., Hasinger, G., Lewin, W. H. G., Magnier, E. A., van Paradijs, J., Pietsch, W., Read, A. M., & Trümper, J. 2001, A&A, 373, 63
- Trinchieri, G., Fabbiano, G., & Peres, G. 1988, ApJ, 325, 531
- Yokogawa, J., Kensuke Imanishi, M. T., Nishiuchi, M., & Koyama, K. 2000, ApJS, 128, 491

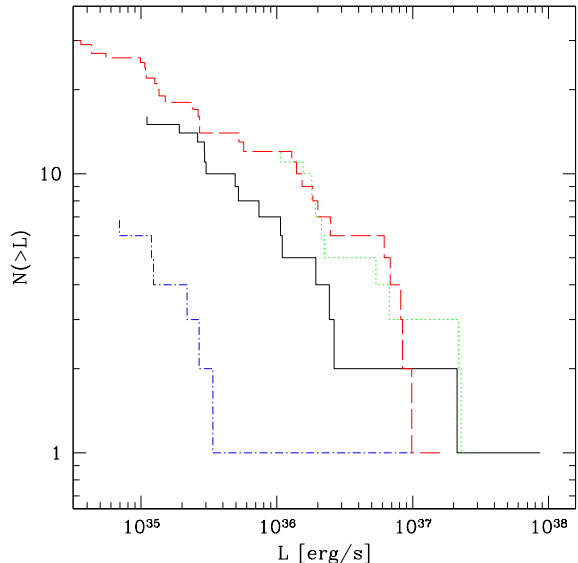


Fig. 8.— Observed luminosity function of radio SNR in M33 combined from the three *Chandra* observations. For comparison we show the observed luminosity of the Magellanic Clouds (dot-dashed histogram—SMC, dashed histogram—LMC) from Sasaki et al. (2000a) and Sasaki et al. (2000b), and of M31 (dotted histogram) from Supper et al. (2001).

Table 3. Source list ordered with increasing right ascension.

Source CXO J	Coord./Unc. RA/Dec/["]	ObsId	Counts						Flux[10^{-7} cts/s/cm 2] ^a			L [erg/s] ^a 0.3-8.0
			0.3-8.0	0.3-2.0	2.0-8.0	0.3-1.0	1.0-2.1	2.1-8.0	0.3-8.0	0.3-2.0	2.0-8.0	
013219.6+304153	01:32:19.668	1730	8.2(4.3)	<7.5	6.9(4.0)	—	—	—	8.6(4.4)	<5.6	8.4(3.4)	1.54e+35
	30:41:53.57	786	—	—	—	—	—	—	—	—	—	—
	27.0	2023	—	—	—	—	—	—	—	—	—	—
013239.7+303245	01:32:39.787	1730	11.0 ^b (3.3)	<9.3	9.6(4.7)	—	—	—	8.2 ^b	<7.0	9.6(3.6)	1.47e+35 ^b
	30:32:45.78	786	—	—	—	—	—	—	—	—	—	—
	12.7	2023	—	—	—	—	—	—	—	—	—	—
013253.4+303817	01:32:53.481	1730	969.6(32.8)	703.5(27.8)	237.5(17.1)	226.9(16.3)	492.8(23.4)	246.9(17.7)	800(27)	560(21)	220(15)	1.43e+37
	30:38:17.07	786	—	—	—	—	—	—	—	—	—	—
	2.6	2023	—	—	—	—	—	—	—	—	—	—
013253.9+303312	01:32:53.931	1730	665.4(28.5)	584.9(26.3)	146.2(15.2)	216.1(16.4)	315.7(19.3)	140.7(14.7)	440(19)	350(15)	150(14)	7.79e+36
	30:33:12.29	786	—	—	—	—	—	—	—	—	—	—
	3.0	2023	—	—	—	—	—	—	—	—	—	—
013256.3+303558	01:32:56.324	1730	<43.1	<14.3	20.5(8.2)	—	—	—	<32.3	<10.7	18(6.5)	<5.78e+35
	30:35:58.64	786	—	—	—	—	—	—	—	—	—	—
	5.6	2023	—	—	—	—	—	—	—	—	—	—
013308.3+304802	01:33:08.375	1730	—	—	—	—	—	—	—	—	—	—
	30:48:02.69	786	127.2(15.0)	136.3(14.3)	21.0 ^b (4.6)	39.3(8.5)	65.9(9.9)	11.2(8.8)	66(8.4)	67(7.3)	15.7 ^b	1.19e+36
	2.5	2023	<6.0	<6.6	<4.6	—	—	—	<4.5	<5.0	<3.5	<8.10e+34
013315.1+305317	01:33:15.139	1730	—	—	—	—	—	—	—	—	—	—
	30:53:17.94	786	4824.9(74.1)	3852.6(64.5)	929.0(36.7)	1216.3(37.7)	2778.4(54.7)	818.7(35.1)	3000(46)	2200(36)	900(36)	5.33e+37
	0.7	2023	9210.7(99.3)	6994.6(85.6)	2167.0(50.2)	1550.3(41.4)	5705.2(77.0)	2059.4(48.8)	5800(62)	4100(50)	1700(38)	1.03e+38
013315.5+304448	01:33:15.584	1730	215.7(20.8)	170.9(16.3)	44.8(13.7)	44.9(8.6)	95.3(11.4)	31.6(9.6)	180(18)	140(13)	44(12)	3.28e+36
	30:44:48.28	786	200.9(22.8)	174.9(18.2)	25.9(14.7)	34.5(8.9)	91.5(11.5)	20.4(9.9)	170(19)	130(14)	33(14)	2.99e+36
	1.5	2023	<5.7	<4.6	<6.0	—	—	—	<4.3	<3.5	<4.5	<7.70e+34
013320.5+304646	01:33:20.522	1730	<12.2	<4.6	3.5(3.2)	—	—	—	<9.2	<3.5	3.1(1.8)	<1.65e+35
	30:46:46.36	786	<6.0	<6.6	<4.6	—	—	—	<4.5	<5.0	<3.5	<8.10e+34
	2.4	2023	<6.0	<6.6	<4.6	—	—	—	<4.5	<5.0	<3.5	<8.10e+34
013321.7+303858	01:33:21.716	1730	31.0(6.8)	<12.2	26.6(6.4)	0.6(2.3)	4.6(3.4)	25.8(6.3)	24(5.2)	<9.2	21(4.2)	4.25e+35
	30:38:58.24	786	—	—	—	—	—	—	—	—	—	—
	1.4	2023	<8.3	<7.5	<6.0	—	—	—	<6.2	<5.6	<4.5	<1.11e+35
013321.9+303921	01:33:21.943	1730	28.5(6.6)	14.5(5.0)	13.9(5.0)	2.5(2.9)	13.5(4.8)	12.4(4.8)	22(5.0)	11(2.9)	11(3.0)	3.86e+35
	30:39:21.12	786	—	—	—	—	—	—	—	—	—	—
	1.4	2023	<5.7	<6.0	<4.6	—	—	—	<4.3	<4.5	<3.5	<7.70e+34
013323.8+303517	01:33:23.887	1730	21.3(6.0)	13.1(4.8)	10.9(5.4)	3.3(3.2)	9.5(4.3)	8.7(4.3)	17(4.6)	10(2.9)	9.0(3.4)	2.97e+35
	30:35:17.36	786	—	—	—	—	—	—	—	—	—	—
	1.6	2023	—	—	—	—	—	—	—	—	—	—
013323.9+304821	01:33:23.996	1730	—	—	—	—	—	—	—	—	—	—
	30:48:21.74	786	57.2(9.6)	35.5(7.8)	27.3(7.8)	2.7(3.6)	31.0(6.8)	26.3(6.8)	46(7.4)	27(5.8)	25(6.6)	8.15e+35
	3.2	2023	<12.2	<6.6	<12.2	—	—	—	<9.2	<5.0	<9.2	<1.65e+35
013324.4+304401	01:33:24.447	1730	2023.7(46.1)	1339.0(37.6)	689.3(27.4)	313.9(18.8)	1067.9(33.7)	643.2(26.5)	1700(39)	1100(31)	590(23)	3.03e+37
	30:44:01.47	786	3864.0(63.3)	2629.1(52.3)	1233.8(36.3)	708.2(27.7)	2018.7(46.0)	1137.8(34.9)	2800(45)	1800(37)	960(28)	4.95e+37
	0.7	2023	7800.0(93.0)	5672.6(78.0)	2016.8(49.7)	1984.4(48.1)	3929.4(64.9)	1867.2(48.7)	2500(31)	1700(23)	1000(25)	4.56e+37
013324.7+304210	01:33:24.799	1730	<9.7	<4.6	<12.2	—	—	—	<7.3	<3.5	<9.2	<1.31e+35
	30:42:10.73	786	8.0(4.4)	<12.2	<14.2	—	—	—	5.7(3.1)	<9.2	<10.7	1.02e+35
	1.3	2023	<6.6	<4.6	<7.5	—	—	—	<5.0	<3.5	<5.6	<9.00e+34

Table 3—Continued

Source CXO J	Coord./Unc. RA/Dec/["]	ObsId	Counts							Flux[10^{-7} cts/s/cm 2] ^a			L [erg/s] ^a 0.3-8.0
			0.3-8.0	0.3-2.0	2.0-8.0	0.3-1.0	1.0-2.1	2.1-8.0	0.3-8.0	0.3-2.0	2.0-8.0		
013325.5+303618	01:33:25.569	1730	24.6(6.3)	15.0(5.1)	10.0 ^b (3.2)	3.4(3.2)	11.5(4.6)	9.8(4.4)	19(4.8)	11(3.0)	7.5 ^b	3.36e+35	—
	30:36:18.15	786	—	—	—	—	—	—	—	—	—	—	
	1.4	2023	—	—	—	—	—	—	—	—	—	—	
013325.5+304439	01:33:25.582	1730	12.0 ^b (3.5)	9.0 ^b (3.0)	<13.4	—	—	—	9.0 ^b	6.7 ^b	<10.1	1.61e+35 ^b	—
	30:44:39.95	786	13.8(6.0)	<17.8	<18.2	—	—	—	10(4.2)	<13.4	<13.7	1.78e+35	
	1.6	2023	<6.6	<7.5	<4.6	—	—	—	<5.0	<5.6	<3.5	<9.00e+34	
013325.6+304756	01:33:25.641	1730	—	—	—	—	—	—	—	—	—	—	—
	30:47:56.28	786	16.8(6.5)	11.1(5.5)	5.0 ^b (2.2)	—	—	—	13(4.8)	8.5(4.0)	3.8 ^b	2.38e+35	
	2.8	2023	<4.6	<4.6	<4.6	—	—	—	<3.5	<3.5	<3.5	<6.30e+34	
013326.0+304119	01:33:26.062	1730	<10.2	3.9(3.2)	<4.6	—	—	—	<7.7	2.9(1.5)	<3.5	<1.38e+35	—
	30:41:19.01	786	<6.6	<6.6	<4.6	—	—	—	<5.0	<5.0	<3.5	<9.00e+34	
	1.2	2023	<15.7	<13.8	<7.5	—	—	—	<11.8	<10.4	<5.6	<2.11e+35	
013327.6+304045	01:33:27.647	1730	<12.2	3.8(3.2)	<6.6	—	—	—	<9.2	2.7(1.5)	<5.0	<1.65e+35	—
	30:40:45.82	786	<4.6	<4.6	<4.6	—	—	—	<3.5	<3.5	<3.5	<6.30e+34	
	1.1	2023	<9.7	<9.1	<6.0	—	—	—	<7.3	<6.8	<4.5	<1.31e+35	
013327.7+304645	01:33:27.728	1730	18.0(5.4)	16.5(5.2)	<9.1	—	—	—	14(4.3)	13(3.2)	<6.8	2.52e+35	—
	30:46:45.84	786	25.0(7.2)	24.9(6.7)	<9.8	16.1(5.5)	9.2(4.4)	0.9(3.8)	20(5.4)	18(4.8)	<7.4	3.49e+35	
	1.3	2023	122.5(15.0)	90.5(12.0)	33.0 ^b (5.7)	43.4(8.8)	43.6(8.8)	28.6(9.8)	52(6.6)	38(5.1)	24.7 ^b	9.21e+35	
013327.9+303135	01:33:27.922	1730	18.7(6.1)	17.8(5.8)	<9.3	—	—	—	15(4.9)	15(3.8)	<7.0	2.77e+35	—
	30:31:35.77	786	—	—	—	—	—	—	—	—	—	—	
	2.3	2023	—	—	—	—	—	—	—	—	—	—	
013328.6+304321	01:33:28.686	1730	26.5(6.4)	5.8(3.6)	7.7(4.0)	6.7(3.8)	6.7(3.8)	13.0(4.8)	20(4.7)	4.3(1.8)	5.8(2.1)	3.50e+35	—
	30:43:21.30	786	28.4(7.2)	17.1(5.3)	<18.0	5.7(4.0)	16.6(5.3)	6.0(4.4)	19(4.9)	11(3.6)	<13.5	3.47e+35	
	1.2	2023	<4.6	<4.6	<4.6	—	—	—	<3.5	<3.5	<3.5	<6.30e+34	
013328.7+304746	01:33:28.786	1730	—	—	—	—	—	—	—	—	—	—	—
	30:47:46.01	786	70.0(10.9)	61.7(9.6)	<19.8	47.3(8.4)	18.0(5.8)	7.2(5.7)	53(8.0)	45(6.8)	<14.9	9.46e+35	
	2.4	2023	80.8(14.7)	60.6(9.7)	<25.3	66.3(10.5)	8.6(6.7)	-3.1(9.3)	33(6.6)	26(4.2)	<19.0	5.85e+35	
013329.0+304216	01:33:29.009	1730	199.4(15.2)	202.2(15.3)	<6.0	140.7(12.9)	58.7(8.7)	-0.1(2.3)	150(12)	150(11)	<4.5	2.72e+36	—
	30:42:16.54	786	242.5(16.7)	240.6(16.6)	<10.2	180.8(14.5)	60.3(8.9)	1.3(3.2)	160(11)	160(11)	<7.7	2.93e+36	
	1.0	2023	615.1(31.4)	610.5(28.6)	<37.1	512.3(25.7)	96.1(13.6)	0.4(14.3)	200(10)	180(8.6)	<27.8	3.61e+36	
013329.2+304537	01:33:29.278	1730	44.1(7.9)	30.3(6.6)	12.6(4.8)	5.5(3.6)	26.4(6.3)	12.1(4.8)	34(6.0)	23(4.2)	9.8(2.9)	6.01e+35	—
	30:45:37.10	786	55.1(9.3)	34.3(7.2)	21.6(6.4)	2.7(3.6)	32.0(6.9)	20.9(6.4)	39(6.5)	24(5.0)	17(4.9)	7.00e+35	
	1.6	2023	<8.3	<4.6	<9.1	—	—	—	<6.2	<3.5	<6.8	<1.11e+35	
013329.2+304508	01:33:29.299	1730	188.3(14.9)	123.1(12.2)	67.0(9.5)	30.3(6.6)	98.3(11.0)	59.5(8.9)	140(11)	93(8.4)	52(6.5)	2.55e+36	—
	30:45:08.07	786	243.9(17.0)	171.4(14.3)	70.1(9.7)	60.4(9.0)	115.4(11.9)	68.4(9.7)	170(12)	120(9.7)	53(7.3)	3.05e+36	
	1.1	2023	351.2(24.7)	207.9(17.6)	80.0 ^b (8.9)	113.1(14.4)	151.8(14.9)	82.8(15.0)	120(8.2)	60(5.1)	60.0 ^b	2.06e+36	
013329.4+304912	01:33:29.434	1730	—	—	—	—	—	—	—	—	—	—	—
	30:49:12.03	786	103.0(12.8)	103.7(11.9)	<12.1	85.5(10.7)	21.5(6.2)	1.8(5.3)	82(9.8)	78(8.9)	<9.1	1.47e+36	
	1.7	2023	186.0(18.9)	189.2(16.7)	<35.2	127.1(13.5)	46.4(9.7)	2.7(10.6)	80(8.5)	82(7.3)	<26.4	1.42e+36	
013330.5+303404	01:33:30.588	1730	64.5(9.2)	23.6(6.2)	54.6(8.6)	1.4(2.7)	20.5(5.7)	42.8(7.7)	50(7.2)	19(4.0)	44(6.1)	9.02e+35	—
	30:34:04.62	786	—	—	—	—	—	—	—	—	—	—	
	1.5	2023	—	—	—	—	—	—	—	—	—	—	
013330.8+304132	01:33:30.873	1730	<4.6	<4.6	<4.6	—	—	—	<3.5	<3.5	<3.5	<6.30e+34	—
	30:41:32.02	786	6.0 ^b (2.5)	<6.6	5.6(3.6)	—	—	—	4.5 ^b	<5.0	4.0(2.6)	8.06e+34 ^b	
	1.1	2023	<9.7	<7.5	<7.5	—	—	—	<7.3	<5.6	<5.6	<1.31e+35	

Table 3—Continued

Source CXO J	Coord./Unc. RA/Dec/["]	ObsId	Counts						Flux[10^{-7} cts/s/cm 2] ^a			L [erg/s] ^a 0.3–8.0
			0.3–8.0	0.3–2.0	2.0–8.0	0.3–1.0	1.0–2.1	2.1–8.0	0.3–8.0	0.3–2.0	2.0–8.0	
013331.1+303333	01:33:31.161	1730	261.0(17.3)	259.3(17.2)	<11.6	158.7(13.7)	99.0(11.0)	3.5(3.6)	200(13)	200(13)	<8.7	3.61e+36
	30:33:33.51	786	—	—	—	—	—	—	—	—	—	—
	1.1	2023	—	—	—	—	—	—	—	—	—	—
013331.3+303737	01:33:31.366	1730	14.5(5.1)	9.0 ^b (3.0)	<13.8	—	—	—	11(3.7)	6.8 ^b	<10.4	1.90e+35
	30:37:37.54	786	—	—	—	—	—	—	—	—	—	—
	1.1	2023	<9.7	<4.6	<12.2	—	—	—	<7.3	<3.5	<9.2	<1.31e+35
013332.1+303656	01:33:32.112	1730	19.2(5.6)	<11.8	15.5(5.1)	—	—	—	14(4.1)	<8.9	12(3.0)	2.53e+35
	30:36:56.47	786	—	—	—	—	—	—	—	—	—	—
	1.1	2023	—	—	—	—	—	—	—	—	—	—
013333.0+304920	01:33:33.008	1730	—	—	—	—	—	—	—	—	—	—
	30:49:20.38	786	35.6(8.1)	22.0(6.9)	13.0 ^b (3.6)	2.8(3.6)	21.0(5.9)	13.4(5.6)	28(6.0)	17(5.0)	9.8 ^b	4.94e+35
	3.0	2023	<9.1	<6.6	<7.5	—	—	—	<6.8	<5.0	<5.6	<1.22e+35
013333.6+303108	01:33:33.606	1730	86.3(10.9)	50.5(8.6)	38.5(7.7)	9.5(4.6)	41.2(7.6)	36.5(7.5)	70(8.7)	40(6.0)	32(5.5)	1.25e+36
	30:31:08.76	786	—	—	—	—	—	—	—	—	—	—
	2.2	2023	—	—	—	—	—	—	—	—	—	—
013333.9+303938	01:33:33.924	1730	3.9(3.2)	<8.5	<8.5	—	—	—	2.8(2.3)	<6.4	<6.4	4.93e+34
	30:39:38.97	786	<4.6	<4.6	<4.6	—	—	—	<3.5	<3.5	<3.5	<6.30e+34
	1.0	2023	<6.6	<7.5	<4.6	—	—	—	<5.0	<5.6	<3.5	<9.00e+34
013334.1+303714	01:33:34.112	1730	59.1(8.8)	36.4(7.1)	23.9(6.1)	4.7(3.4)	30.8(6.6)	23.5(6.0)	43(6.4)	26(4.4)	18(3.7)	7.71e+35
	30:37:14.3	786	—	—	—	—	—	—	—	—	—	—
	1.0	2023	<5.7	<4.6	<6.0	—	—	—	<4.3	<3.5	<4.5	<7.70e+34
013334.1+303210	01:33:34.155	1730	5036.7(72.1)	3691.1(61.8)	1348.6(37.9)	899.7(31.1)	2900.9(54.9)	1238.0(36.3)	4100(59)	3000(49)	1100(31)	7.37e+37
	30:32:10.51	786	—	—	—	—	—	—	—	—	—	—
	0.7	2023	—	—	—	—	—	—	—	—	—	—
013334.5+303556	01:33:34.525	1730	18.1(5.4)	17.0 ^b (4.1)	<8.5	—	—	—	13(4.0)	12.8 ^b	<6.4	2.39e+35
	30:35:56.22	786	—	—	—	—	—	—	—	—	—	—
	1.1	2023	—	—	—	—	—	—	—	—	—	—
013335.1+304451	01:33:35.152	1730	<4.6	<4.6	<4.6	—	—	—	<3.5	<3.5	<3.5	<6.30e+34
	30:44:51.71	786	<11.1	4.3(3.4)	<4.6	—	—	—	<8.3	3.0(2.3)	<3.5	<1.49e+35
	1.2	2023	<9.7	<9.1	<6.0	—	—	—	<7.3	<6.8	<4.5	<1.31e+35
013335.5+303728	01:33:35.502	1730	16.2(5.2)	9.7(4.3)	6.0 ^b (2.5)	—	—	—	12(4.0)	7.4(2.4)	4.5 ^b	2.21e+35
	30:37:28.84	786	38.1(7.5)	24.4(6.2)	12.2(4.8)	13.2(4.8)	12.5(4.7)	12.6(4.8)	19(3.7)	11(2.9)	8.8(3.5)	3.43e+35
	1.0	2023	<5.7	<6.0	<4.6	—	—	—	<4.3	<4.5	<3.5	<7.70e+34
013335.8+304654	01:33:35.830	1730	8.1(4.3)	<12.2	<12.2	—	—	—	6.4(3.4)	<9.2	<9.2	1.14e+35
	30:46:54.65	786	<14.6	<6.0	<12.6	—	—	—	<11.0	<4.5	<9.5	<1.97e+35
	1.6	2023	<4.6	<4.6	<4.6	—	—	—	<3.5	<3.5	<3.5	<6.30e+34
013335.9+303627	01:33:35.962	1730	100.4(11.2)	96.6(10.9)	<13.8	62.3(9.0)	35.5(7.1)	2.7(3.2)	76(8.4)	72(7.4)	<10.4	1.35e+36
	30:36:27.35	786	—	—	—	—	—	—	—	—	—	—
	1.0	2023	—	—	—	—	—	—	—	—	—	—
013336.0+303333	01:33:36.094	1730	24.0(6.3)	19.9(5.8)	<14.2	5.2(3.6)	15.4(5.1)	3.5(3.4)	18(4.8)	15(3.6)	<10.7	3.28e+35
	30:33:33.43	786	—	—	—	—	—	—	—	—	—	—
	1.4	2023	—	—	—	—	—	—	—	—	—	—
013336.3+303742	01:33:36.398	1730	118.1(11.9)	71.6(9.5)	47.5(8.0)	6.8(3.8)	64.8(9.1)	46.6(7.9)	90(9.1)	54(6.4)	37(5.4)	1.60e+36
	30:37:42.26	786	98.6(11.2)	62.5(9.1)	38.7(7.5)	10.8(4.6)	49.2(8.1)	38.9(7.5)	48(5.5)	28(4.1)	27(5.2)	8.63e+35
	1.0	2023	<9.7	<9.1	<6.0	—	—	—	<7.3	<6.8	<4.5	<1.31e+35

Table 3—Continued

Source CXO J	Coord./Unc. RA/Dec/["]	ObsId	Counts						Flux[10^{-7} cts/s/cm 2] ^a			L [erg/s] ^a	
			0.3–8.0	0.3–2.0	2.0–8.0	0.3–1.0	1.0–2.1	2.1–8.0	0.3–8.0	0.3–2.0	2.0–8.0	0.3–8.0	0.3–8.0
013336.6+303729	01:33:36.694	1730	17.4(5.3)	10.8(4.4)	6.6(3.8)	—	—	—	13(4.0)	8.1(2.5)	5.0(2.0)	2.36e+35	
	30:37:29.22	786	14.1(5.1)	5.5(3.6)	7.0 ^b (2.7)	—	—	—	6.6(2.4)	2.4(1.6)	5.3 ^b	1.19e+35	
	1.0	2023	<11.1	<6.0	<12.2	—	—	—	<8.3	<4.5	<9.2	<1.49e+35	
013337.4+304718	01:33:37.490	1730	92.0(10.9)	68.8(9.5)	26.0(6.5)	17.1(5.3)	49.0(8.1)	25.8(6.5)	71(8.4)	53(6.5)	20(4.2)	1.27e+36	
	30:47:18.27	786	145.3(13.7)	104.8(11.5)	38.9(8.1)	28.5(6.7)	80.9(10.2)	36.7(7.7)	100(9.7)	73(8.0)	31(6.3)	1.85e+36	
	1.2	2023	75.3(12.3)	42.7(9.5)	41.0 ^b (6.4)	6.2(5.4)	27.3(7.3)	33.6(9.5)	29(5.2)	16(3.9)	30.7 ^b	5.13e+35	
013337.6+304010	01:33:37.659	1730	7.0 ^b (2.7)	<13.8	<9.1	—	—	—	5.3 ^b	<10.4	<6.8	9.51e+34 ^b	
	30:40:10.18	786	22.1(6.7)	8.6(4.3)	<13.8	14.1(5.2)	4.1(3.6)	4.0(4.1)	10(3.2)	3.7(1.8)	<10.4	1.86e+35	
	1.0	2023	<9.7	<6.0	<9.1	—	—	—	<7.3	<4.5	<6.8	<1.31e+35	
013337.8+303837	01:33:37.892	1730	6.6(3.8)	<4.6	6.8(3.8)	—	—	—	4.7(2.7)	<3.5	5.0(1.9)	8.45e+34	
	30:38:37.49	786	11.5(4.8)	<9.1	9.3(4.4)	—	—	—	5.3(2.2)	<6.8	6.1(2.9)	9.51e+34	
	1.0	2023	<11.1	<12.2	<6.0	—	—	—	<8.3	<9.2	<4.5	<1.49e+35	
013337.9+304023	01:33:37.964	1730	7.8(4.0)	<10.1	5.0 ^b (2.2)	—	—	—	5.4(2.8)	<7.6	3.8 ^b	9.69e+34	
	30:40:23.52	786	6.0 ^b (2.5)	<9.1	<12.2	—	—	—	4.5 ^b	<6.8	<9.2	8.06e+34 ^b	
	1.0	2023	<6.6	<4.6	<7.5	—	—	—	<5.0	<3.5	<5.6	<9.00e+34	
013337.9+304035	01:33:37.992	1730	21.7(5.8)	7.9(4.0)	13.8(4.8)	<1.9	8.9(4.1)	12.8(4.7)	15(4.0)	5.5(2.0)	9.6(2.6)	2.70e+35	
	30:40:35.58	786	11.6(4.7)	<13.8	6.1(3.8)	—	—	—	13(5.1)	<10.4	10(5.9)	2.40e+35	
	1.0	2023	<11.1	<12.2	<6.0	—	—	—	<8.3	<9.2	<4.5	<1.49e+35	
013339.2+304049	01:33:39.212	1730	72.6(9.6)	41.9(7.5)	29.7(6.5)	6.9(3.8)	36.9(7.1)	28.7(6.5)	50(6.7)	29(4.5)	21(3.8)	9.01e+35	
	30:40:49.48	786	42.5(7.8)	30.9(6.7)	12.1(4.7)	3.9(3.2)	28.8(6.5)	11.4(4.6)	47(8.4)	32(6.8)	17(6.4)	8.48e+35	
	1.0	2023	<8.3	<9.1	<4.6	—	—	—	<6.2	<6.8	<3.5	<1.11e+35	
013339.8+304350	01:33:39.807	1730	6.7(3.8)	<8.5	5.0 ^b (2.2)	—	—	—	4.9(2.8)	<6.4	3.8 ^b	8.78e+34	
	30:43:50.17	786	9.0(4.3)	<16.5	<9.1	—	—	—	6.0(2.8)	<12.4	<6.8	1.07e+35	
	1.0	2023	<4.6	<4.6	<4.6	—	—	—	<3.5	<3.5	<3.5	<6.30e+34	
013340.0+304323	01:33:40.084	1730	45.1(7.8)	26.7(6.3)	18.0 ^b (4.2)	11.8(4.6)	16.8(5.2)	16.3(5.2)	32(5.6)	19(3.7)	13.5 ^b	5.71e+35	
	30:43:23.11	786	35.7(7.1)	24.3(6.1)	12.2(5.0)	1.6(2.7)	23.8(6.0)	10.2(4.4)	23(4.7)	16(3.9)	8.5(3.5)	4.19e+35	
	1.0	2023	<12.6	<12.2	<7.5	—	—	—	<9.5	<9.2	<5.6	<1.70e+35	
013340.7+303523	01:33:40.785	1730	14.1(5.0)	9.5(4.3)	5.0 ^b (2.2)	—	—	—	10(3.6)	6.9(2.3)	<3.8	1.85e+35	
	30:35:23.54	786	<13.8	4.5(3.4)	<6.0	—	—	—	<10.4	5.7(4.0)	<4.5	<1.86e+35	
	1.1	2023	—	—	—	—	—	—	—	—	—	—	
013341.2+303950	01:33:41.216	1730	<4.6	<4.6	<4.6	—	—	—	<3.5	<3.5	<3.5	<6.30e+34	
	30:39:50.48	786	4.7(3.6)	<9.1	<9.1	—	—	—	2.1(1.6)	<6.8	<6.8	3.81e+34	
	1.0	2023	<5.7	<6.0	<4.6	—	—	—	<4.3	<4.5	<3.5	<7.70e+34	
013341.4+303815	01:33:41.447	1730	7.7(4.0)	<8.5	5.8(3.6)	—	—	—	5.4(2.8)	<6.4	4.2(1.7)	9.69e+34	
	30:38:15.99	786	<4.6	<4.6	<4.6	—	—	—	<3.5	<3.5	<3.5	<6.30e+34	
	1.0	2023	<6.6	<4.6	<7.5	—	—	—	<5.0	<3.5	<5.6	<9.00e+34	
013341.5+303220	01:33:41.505	1730	21.3(6.1)	15.4(5.2)	<15.7	8.0(4.1)	7.3(4.0)	6.2(4.0)	17(4.7)	12(3.2)	<11.8	2.96e+35	
	30:32:20.5	786	—	—	—	—	—	—	—	—	—	—	
	1.5	2023	—	—	—	—	—	—	—	—	—	—	
013341.5+304136	01:33:41.528	1730	37.6(7.2)	21.8(5.8)	18.6(5.4)	0.9(2.3)	19.9(5.6)	16.7(5.2)	26(5.0)	15(3.2)	13(3.0)	4.65e+35	
	30:41:36.23	786	56.1(8.6)	34.3(7.0)	22.5(5.9)	9.8(4.3)	23.9(6.0)	22.5(5.9)	37(5.6)	22(4.5)	16(4.1)	6.56e+35	
	1.0	2023	<14.2	<7.5	<12.2	—	—	—	<10.7	<5.6	<9.2	<2.95e+35	
013341.8+303848	01:33:41.885	1730	99.6(11.0)	95.7(10.8)	5.9(3.6)	63.9(9.0)	29.9(6.5)	5.8(3.6)	70(7.8)	67(6.9)	4.2(1.7)	1.25e+36	
	30:38:48.71	786	318.8(18.9)	318.6(18.9)	<9.1	236.3(16.4)	81.6(10.1)	0.9(2.7)	150(8.7)	130(8.0)	<6.8	2.61e+36	
	1.0	2023	623.0(31.1)	312.5(20.1)	44.0 ^b (6.6)	401.2(23.2)	176.5(16.3)	35.0(14.9)	200(10)	92(6.0)	33.0 ^b	3.57e+36	

Table 3—Continued

Source CXO J	Coord./Unc. RA/Dec./["]	ObsId	Counts						Flux[10^{-7} cts/s/cm 2] ^a			L [erg/s] ^a 0.3–8.0
			0.3–8.0	0.3–2.0	2.0–8.0	0.3–1.0	1.0–2.1	2.1–8.0	0.3–8.0	0.3–2.0	2.0–8.0	
013342.5+304253	01:33:42.508	1730	19.6(5.6)	12.8(4.7)	8.7(4.1)	—	—	—	15(4.2)	9.7(2.7)	6.6(2.3)	2.65e+35
	30:42:53.11	786	87.3(10.5)	35.2(7.1)	50.9(8.3)	2.3(2.9)	38.5(7.3)	46.3(8.0)	56(6.8)	22(4.5)	35(5.7)	1.01e+36
	1.0	2023	<15.7	7.0 ^b (2.7)	<4.6	—	—	—	<11.8	<5.3	<3.5	<2.11e+35
013342.7+304642	01:33:42.741	1730	9.7(4.4)	5.0 ^b (2.2)	5.5(3.6)	—	—	—	19(7.9)	3.8 ^b	11(4.5)	3.34e+35
	30:46:42.14	786	33.9(7.8)	14.5(5.4)	21.8(6.6)	4.2(3.8)	10.3(4.6)	20.2(6.2)	25(5.6)	10(3.8)	18(5.2)	4.51e+35
	1.4	2023	<12.2	<6.6	<9.1	—	—	—	<9.2	<5.0	<6.8	<1.65e+35
013343.4+304630	01:33:43.428	1730	8.8(4.4)	10.4(4.4)	<4.6	—	—	—	20(8.8)	21(6.6)	<3.5	3.60e+35
	30:46:30.83	786	86.1(10.9)	79.7(10.2)	<16.8	70.2(9.6)	10.3(4.6)	6.0(4.6)	61(7.7)	55(7.0)	<12.6	1.09e+36
	1.1	2023	158.4(17.5)	174.6(16.2)	<12.2	154.0(14.5)	32.8(8.1)	<7.5	79(7.5)	75(6.4)	<9.2	1.42e+36
013343.5+304102	01:33:43.534	1730	7.0 ^b (2.7)	8.0 ^b (2.8)	<4.6	—	—	—	5.2 ^b	6.0 ^b	<3.5	9.30e+34 ^b
	30:41:02.97	786	12.1(5.2)	10.6(4.6)	<6.5	—	—	—	5.7(2.4)	4.6(2.0)	<4.9	1.02e+35
	1.0	2023	<5.7	<4.6	<6.0	—	—	—	<4.3	<3.5	<4.5	<7.70e+34
013343.9+303508	01:33:43.938	1730	6.7(3.8)	3.8(3.2)	<10.1	—	—	—	4.9(2.8)	2.8(1.5)	<7.6	8.77e+34
	30:35:08.30	786	<7.5	<7.5	<4.6	—	—	—	<5.6	<5.6	<3.5	<1.00e+35
	1.1	2023	—	—	—	—	—	—	—	—	—	—
013344.2+304026	01:33:44.245	1730	16.0 ^b (4.0)	<14.4	11.0 ^b (3.3)	—	—	—	12.0 ^b	<10.8	8.3 ^b	3.31e+35 ^b
	30:40:26.16	786	41.0 ^b (6.4)	27.5(8.2)	<30.2	—	—	—	30.8 ^b	12(3.5)	<22.7	5.52e+35 ^b
	1.0	2023	<6.6	<4.6	<7.5	—	—	—	<5.0	<3.5	<5.6	<9.00e+34
013346.2+303807	01:33:46.252	1730	<4.6	<4.6	<4.6	—	—	—	<3.5	<3.5	<3.5	<6.30e+34
	30:38:07.18	786	<5.7	<4.6	<6.0	—	—	—	<4.3	<3.5	<4.5	<7.70e+34
	1.0	2023	143.0(19.6)	150.3(18.2)	<6.0	92.5(12.8)	60.8(10.5)	46.7(12.0)	90(9.0)	80(7.7)	<4.5	1.62e+36
013346.5+303748	01:33:46.584	1730	157.4(13.6)	107.8(11.4)	49.7(8.1)	32.8(6.8)	77.9(9.9)	46.7(7.9)	120(10)	80(7.7)	38(5.3)	2.09e+36
	30:37:48.33	786	198.5(15.2)	124.9(12.3)	72.8(9.6)	49.6(8.1)	80.7(10.0)	68.2(9.4)	93(7.1)	54(5.3)	48(6.4)	1.65e+36
	1.0	2023	—	—	—	—	—	—	—	—	—	—
013346.7+304318	01:33:46.781	1730	5.8(3.6)	<10.1	<10.1	—	—	—	4.1(2.6)	<7.6	<7.6	7.35e+34
	30:43:18.09	786	<10.1	<8.5	<6.6	—	—	—	<7.6	<6.4	<5.0	<1.36e+35
	0.9	2023	<9.7	<7.5	<7.5	—	—	—	<7.3	<5.6	<5.6	<1.31e+35
013347.5+304042	01:33:47.574	1730	7.9(4.0)	5.0 ^b (2.2)	<10.1	—	—	—	5.3(2.7)	3.8 ^b	<7.6	9.56e+34
	30:40:42.75	786	13.5(5.0)	11.9(4.7)	<12.2	—	—	—	6.2(2.3)	5.1(2.0)	<9.2	1.11e+35
	1.0	2023	<11.1	<9.1	<7.5	—	—	—	<8.3	<6.8	<5.6	<1.49e+35
013348.6+303304	01:33:48.645	1730	29.0 ^b (5.4)	27.9(6.6)	<9.1	—	—	—	21.8 ^b	21(4.2)	<6.8	3.90e+35 ^b
	30:33:04.70	786	<10.2	8.5(6.4)	<6.0	—	—	—	<7.7	12(4.7)	<4.5	<1.38e+35
	1.3	2023	—	—	—	—	—	—	—	—	—	—
013349.1+304055	01:33:49.122	1730	<8.5	<8.5	<4.6	—	—	—	<6.4	<6.4	<3.5	<1.15e+35
	30:40:55.19	786	6.0 ^b (2.5)	5.7(3.6)	<6.6	—	—	—	4.5 ^b	2.4(1.5)	<5.0	8.06e+34 ^b
	1.0	2023	<9.7	<9.1	<6.0	—	—	—	<7.3	<6.8	<4.5	<1.31e+35
013350.5+303821	01:33:50.520	1730	39.6(7.4)	29.7(6.5)	10.7(4.4)	7.9(4.0)	21.9(5.8)	9.8(4.3)	27(5.1)	20(3.8)	7.4(2.3)	4.88e+35
	30:38:21.42	786	123.4(12.3)	92.8(10.7)	30.0(6.6)	42.2(7.6)	50.5(8.2)	30.6(6.7)	57(5.7)	40(4.6)	20(4.4)	1.02e+36
	1.0	2023	<15.7	6.0 ^b (2.5)	<6.0	—	—	—	<11.8	4.5 ^b	<4.5	<2.11e+35
013351.0+303937 ^c	01:33:51.001	1730	5786.1(77.8)	3471.9(60.4)	2314.3(49.8)	—	—	—	4100(56)	2400(43)	1700(36)	7.37e+37
	30:39:37.62	786	10300.6(104.9)	6874.8(85.4)	3425.8(61.7)	—	—	—	4900(50)	3000(37)	2300(41)	8.68e+37
	0.7	2023	171076.0(415.1)	131846.5(364.4)	39229.5(199.6)	—	—	—	53000(130)	37000(100)	19000(95)	9.40e+38
013352.7+303242	01:33:52.715	1730	<4.6	<4.6	<4.6	—	—	—	<3.5	<3.5	<3.5	<6.30e+34
	30:32:42.21	786	<12.1	<4.6	5.4(4.1)	—	—	—	<9.1	<3.5	4.4(3.1)	<1.63e+35
	1.4	2023	—	—	—	—	—	—	—	—	—	—

Table 3—Continued

Source CXO J	Coord./Unc. RA/Dec/["]	ObsId	Counts						Flux[10^{-7} cts/s/cm 2] ^a			L [erg/s] ^a		
			0.3–8.0	0.3–2.0	2.0–8.0	0.3–1.0	1.0–2.1	2.1–8.0	0.3–8.0	0.3–2.0	2.0–8.0	0.3–8.0	0.3–8.0	
013353.3+304016	01:33:53.361	1730	<6.6	<4.6	<6.6	—	—	—	<5.0	<3.5	<5.0	<9.00e+34		
	30:40:16.02	786	10.2(4.4)	9.6(4.3)	<6.6	—	—	—	4.9(2.1)	4.3(1.9)	<5.0	8.79e+34		
	1.0	2023	<12.6	<13.8	<4.6	—	—	—	<9.5	<10.4	<3.5	<1.70e+35		
013353.5+303317	01:33:53.518	1730	<4.6	<4.6	<4.6	—	—	—	<3.5	<3.5	<3.5	<6.30e+34		
	30:33:17.67	786	<9.7	<4.6	2.9(3.2)	—	—	—	<7.3	<3.5	2.1(2.2)	<1.31e+35		
	1.3	2023	—	—	—	—	—	—	—	—	—	—		
013353.6+303605	01:33:53.662	1730	<13.8	<9.1	<9.1	—	—	—	<10.4	<6.8	<6.8	<1.86e+35		
	30:36:05.79	786	21.7(6.4)	11.0 ^b (3.3)	10.0 ^b (3.2)	7.1(4.1)	4.8(3.6)	9.7(4.7)	9.9(2.9)	8.3 ^b	7.5 ^b	1.76e+35		
	1.0	2023	—	—	—	—	—	—	—	—	—	—		
013353.7+303250	01:33:53.715	1730	<7.5	<4.6	<7.5	—	—	—	<5.6	<3.5	<5.6	<1.00e+35		
	30:32:50.21	786	<11.2	<4.6	4.5(3.8)	—	—	—	<8.4	<3.5	4.0(3.1)	<1.50e+35		
	1.4	2023	—	—	—	—	—	—	—	—	—	—		
013354.5+303523	01:33:54.555	1730	12.5(4.7)	9.8(4.3)	<10.1	—	—	—	9.0(3.4)	7.0(2.3)	<7.6	1.61e+35		
	30:35:23.01	786	7.0 ^b (2.7)	<12.2	<12.2	—	—	—	<5.3	<9.2	<9.2	<9.50e+34		
	1.0	2023	—	—	—	—	—	—	—	—	—	—		
013354.6+304519	01:33:54.651	1730	9.0 ^b (3.0)	9.5(4.3)	<4.6	—	—	—	<6.8	6.9(2.3)	<3.5	<1.22e+35		
	30:45:19.25	786	19.5(6.7)	22.0 ^b (4.7)	<7.1	—	—	—	13(4.6)	16.5 ^b	<5.3	2.40e+35		
	1.1	2023	—	—	—	—	—	—	—	—	—	—		
013354.8+303309	01:33:54.872	1730	154.3(13.6)	157.4(13.7)	<8.3	101.0(11.1)	52.3(8.3)	1.2(2.9)	120(10)	120(9.4)	<6.2	2.07e+36		
	30:33:09.98	786	443.2(23.5)	446.4(22.7)	<15.7	391.5(21.2)	55.1(9.2)	2.4(6.6)	230(12)	210(11)	<11.8	4.08e+36		
	1.1	2023	—	—	—	—	—	—	—	—	—	—		
013355.2+303528	01:33:55.217	1730	6.0 ^b (2.5)	<6.6	4.8(3.4)	—	—	—	4.5 ^b	<5.0	3.5(1.6)	8.06e+34 ^b		
	30:35:28.60	786	14.8(5.5)	<12.6	11.0 ^b (3.3)	—	—	—	7.3(2.6)	<9.5	<8.3	1.30e+35		
	1.0	2023	—	—	—	—	—	—	—	—	—	—		
013355.4+304307	01:33:55.450	1730	<4.6	<4.6	<4.6	—	—	—	<3.5	<3.5	<3.5	<6.30e+34		
	30:43:07.24	786	5.5(3.8)	<9.1	<12.2	—	—	—	4.3(2.7)	<6.8	<9.2	7.64e+34		
	1.0	2023	—	—	—	—	—	—	—	—	—	—		
013355.8+303924	01:33:55.822	1730	7.0 ^b (2.7)	<20.4	<6.6	—	—	—	5.3 ^b	<15.3	<5.0	9.51e+34 ^b		
	30:39:24.41	786	12.4(5.0)	9.0 ^b (3.0)	<12.2	—	—	—	5.8(2.3)	6.8 ^b	<9.2	1.03e+35		
	1.0	2023	<4.6	<4.6	<4.6	—	—	—	<3.5	<3.5	<3.5	<6.30e+34		
013356.3+305353	01:33:56.367	1730	—	—	—	—	—	—	—	—	—	—		
	30:53:53.21	786	—	—	—	—	—	—	—	—	—	—		
	4.9	2023	<15.0	<4.6	7.1(4.6)	—	—	—	<11.3	<3.5	3.8(2.2)	<2.02e+35		
013356.8+303729	01:33:56.809	1730	27.6(6.4)	15.7(5.1)	12.8(4.7)	1.9(2.7)	14.0(4.8)	11.9(4.6)	37(8.4)	21(5.2)	17(4.7)	6.57e+35		
	30:37:29.75	786	183.3(14.7)	127.3(12.4)	56.3(8.7)	46.6(8.0)	82.1(10.2)	54.5(8.6)	83(6.7)	53(5.2)	36(5.7)	1.49e+36		
	1.0	2023	—	—	—	—	—	—	—	—	—	—		
013356.8+303706	01:33:56.828	1730	49.4(8.1)	25.7(6.2)	22.8(5.9)	6.8(3.8)	17.9(5.3)	24.7(6.1)	38(6.2)	20(3.9)	18(3.8)	6.76e+35		
	30:37:06.38	786	85.6(10.5)	61.4(9.1)	27.0(6.6)	28.7(6.5)	33.1(6.9)	23.7(6.2)	38(4.7)	25(3.8)	17(4.2)	6.89e+35		
	1.0	2023	—	—	—	—	—	—	—	—	—	—		
013356.9+303652	01:33:56.933	1730	2.8(2.9)	<8.5	<6.6	—	—	—	2.0(2.1)	<6.4	<5.0	3.56e+34		
	30:36:52.73	786	<4.6	<4.6	<4.6	—	—	—	<3.5	<3.5	<3.5	<6.30e+34		
	1.0	2023	—	—	—	—	—	—	—	—	—	—		
013357.0+303500	01:33:57.033	1730	<10.9	<8.5	<7.5	—	—	—	<8.2	<6.4	<5.6	<1.47e+35		
	30:35:00.70	786	21.0 ^b (4.6)	21.9(8.0)	<15.9	—	—	—	15.8 ^b	9.8(3.5)	<11.9	2.83e+35 ^b		
	1.1	2023	—	—	—	—	—	—	—	—	—	—		

Table 3—Continued

Source CXO J	Coord./Unc. RA/Dec/["]	ObsId	Counts							Flux[10^{-7} cts/s/cm 2] ^a			L [erg/s] ^a 0.3–8.0
			0.3–8.0	0.3–2.0	2.0–8.0	0.3–1.0	1.0–2.1	2.1–8.0	0.3–8.0	0.3–2.0	2.0–8.0		
013357.2+305136	01:33:57.240	1730	—	—	—	—	—	—	—	—	—	—	—
	30:51:36.46	786	32.1(8.2)	24.0(6.7)	8.0 ^b (2.8)	9.0(4.9)	16.9(5.6)	5.0(5.1)	26(6.7)	19(5.4)	6.0 ^b	4.56e+35	
	3.5	2023	58.1(11.0)	25.9(6.8)	31.8(8.2)	11.6(5.6)	17.3(6.0)	31.6(8.5)	25(4.6)	11(2.8)	14(3.5)	4.43e+35	
013357.8+303756	01:33:57.882	1730	8.0 ^b (2.8)	<17.8	<7.5	—	—	—	6.0 ^b	<13.4	<5.6	1.07e+35 ^b	
	30:37:56.85	786	27.0 ^b (5.2)	26.0(7.7)	<15.4	—	—	—	20.3 ^b	11(3.3)	<11.6	3.64e+35 ^b	
	1.0	2023	—	—	—	—	—	—	—	—	—	—	
013358.1+303200	01:33:58.127	1730	40.4(7.7)	<9.7	38.7(7.5)	1.1(2.7)	2.3(2.9)	37.3(7.3)	33(6.3)	<7.3	31(5.2)	5.92e+35	
	30:32:00.73	786	36.9(7.9)	8.0 ^b (2.8)	28.8(7.1)	0.7(3.2)	7.2(4.1)	27.7(6.9)	27(5.9)	6.0 ^b	22(5.5)	4.80e+35	
	2.6	2023	—	—	—	—	—	—	—	—	—	—	
013358.1+303438	01:33:58.189	1730	6.0 ^b (2.5)	<7.5	<12.2	—	—	—	4.5 ^b	<5.6	<9.2	8.06e+34 ^b	
	30:34:38.07	786	19.5(6.1)	11.0 ^b (3.3)	8.0 ^b (2.8)	—	—	—	9.6(3.0)	8.2 ^b	6.0 ^b	1.72e+35	
	1.1	2023	—	—	—	—	—	—	—	—	—	—	
013358.3+304826	01:33:58.320	1730	—	—	—	—	—	—	—	—	—	—	
	30:48:26.94	786	—	—	—	—	—	—	—	—	—	—	
	2.1	2023	29.2(7.4)	13.0 ^b (3.6)	18.0(5.8)	0.8(2.9)	8.2(4.3)	20.7(6.3)	12(3.1)	<0.0	7.5(2.4)	2.19e+35	
013358.4+303333	01:33:58.491	1730	23.1(6.2)	22.9(6.1)	<8.3	14.2(5.0)	7.4(4.0)	1.5(2.9)	17(4.6)	17(3.7)	<6.2	3.08e+35	
	30:33:33.10	786	51.7(10.1)	46.6(8.9)	<21.9	38.7(7.8)	9.8(4.8)	11.4(5.8)	38(6.4)	30(5.3)	<16.4	6.79e+35	
	1.3	2023	—	—	—	—	—	—	—	—	—	—	
013358.4+303624	01:33:58.495	1730	<9.3	<12.2	<4.6	—	—	—	<7.0	<9.2	<3.5	<1.25e+35	
	30:36:24.05	786	17.0 ^b (4.1)	18.8(6.1)	<7.5	—	—	—	12.8 ^b	7.9(2.6)	<5.6	2.29e+35 ^b	
	1.0	2023	—	—	—	—	—	—	—	—	—	—	
013358.8+305004	01:33:58.824	1730	—	—	—	—	—	—	—	—	—	—	
	30:50:04.78	786	118.9(12.4)	65.9(9.4)	48.8(8.3)	9.1(4.6)	58.2(8.8)	50.4(8.6)	93(9.8)	51(7.4)	40(6.8)	1.67e+36	
	1.5	2023	88.7(11.2)	47.8(8.3)	38.1(7.5)	3.2(3.6)	47.8(8.1)	38.2(7.8)	36(4.5)	19(3.3)	16(3.2)	6.48e+35	
013359.0+303425	01:33:59.076	1730	<16.5	<12.6	<12.6	—	—	—	<12.4	<9.5	<9.5	<2.39e+35	
	30:34:25.84	786	27.2(8.1)	47.2(9.5)	<7.5	29.9(7.1)	2.0(3.6)	<3.8	14(4.0)	22(4.3)	<5.6	2.50e+35	
	1.2	2023	—	—	—	—	—	—	—	—	—	—	
013359.4+303104	01:33:59.452	1730	—	—	—	—	—	—	—	—	—	—	
	30:31:04.6	786	43.3(10.3)	25.0 ^b (5.0)	18.0 ^b (4.2)	5.7(5.5)	21.8(6.5)	12.4(7.3)	32(8.1)	18.8 ^b	13.5 ^b	5.66e+35	
	2.0	2023	—	—	—	—	—	—	—	—	—	—	
013400.0+303057	01:34:00.081	1730	—	—	—	—	—	—	—	—	—	—	
	30:30:57.01	786	22.0 ^b (4.7)	16.9(6.0)	6.0 ^b (2.5)	—	—	—	16.5 ^b	13(4.7)	4.5 ^b	3.18e+35 ^b	
	2.0	2023	—	—	—	—	—	—	—	—	—	—	
013400.1+305218	01:34:00.186	1730	—	—	—	—	—	—	—	—	—	—	
	30:52:18.15	786	<4.6	<4.6	<4.6	—	—	—	<3.5	<3.5	<3.5	<6.30e+34	
	3.2	2023	18.9(8.7)	<18.0	16.3(6.6)	—	—	—	9.3(3.7)	<13.5	7.9(2.9)	1.67e+35	
013400.2+304218	01:34:00.286	1730	11.2(4.6)	16.4(5.2)	<6.6	—	—	—	8.1(3.3)	12(3.0)	<5.0	1.46e+35	
	30:42:18.05	786	52.0(10.6)	53.0(9.1)	<17.4	42.0(8.3)	8.8(5.1)	2.7(5.7)	25(5.0)	23(4.0)	<13.1	4.54e+35	
	1.0	2023	—	—	—	—	—	—	—	—	—	—	
013400.5+305203	01:34:00.506	1730	—	—	—	—	—	—	—	—	—	—	
	30:52:03.39	786	<4.6	<4.6	<4.6	—	—	—	<3.5	<3.5	<3.5	<6.30e+34	
	3.1	2023	<22.0	11.5(5.0)	<7.4	—	—	—	<16.5	5.0(2.1)	<5.6	<3.18e+35	
013400.7+304138	01:34:00.794	1730	<4.6	<4.6	<4.6	—	—	—	<3.5	<3.5	<3.5	<6.30e+34	
	30:41:38.38	786	<9.1	<5.7	1.7(3.2)	—	—	—	<6.8	<4.3	1.3(2.3)	<1.22e+35	
	1.0	2023	—	—	—	—	—	—	—	—	—	—	

Table 3—Continued

Table 3—Continued

Source CXO J	Coord./Unc. RA/Dec/["]	ObsId	Counts						Flux[10^{-7} cts/s/cm 2] ^a			L [erg/s] ^a	
			0.3–8.0	0.3–2.0	2.0–8.0	0.3–1.0	1.0–2.1	2.1–8.0	0.3–8.0	0.3–2.0	2.0–8.0	0.3–8.0	0.3–8.0
013407.4+303707	01:34:07.471	1730	<12.2	4.7(3.4)	<4.6	—	—	—	<9.2	3.3(1.6)	<3.5	<1.65e+35	—
	30:37:07.43	786	8.0 ^b (2.8)	9.0 ^b (3.0)	<4.6	—	—	—	6.0 ^b	<6.8	<3.5	1.07e+35 ^b	—
	1.1	2023	—	—	—	—	—	—	—	—	—	—	—
013407.6+303902	01:34:07.639	1730	8.7(4.1)	<8.5	6.7(3.8)	—	—	—	6.2(2.9)	<6.4	4.8(1.9)	1.11e+35	—
	30:39:02.19	786	18.8(5.8)	8.8(4.3)	10.8(4.7)	—	—	—	8.7(2.7)	3.7(1.8)	7.3(3.2)	1.55e+35	—
	1.0	2023	<4.6	<4.6	<4.6	—	—	—	<3.5	<3.5	<3.5	<6.30e+34	—
013407.8+303553	01:34:07.811	1730	43.4(7.8)	31.2(6.7)	12.4(4.7)	9.6(4.3)	21.7(5.8)	12.2(4.7)	31(5.6)	2.2(4.1)	8.9(2.6)	5.57e+35	—
	30:35:53.76	786	71.1(10.5)	52.8(9.1)	20.2(6.6)	23.7(6.5)	32.5(7.1)	16.2(6.1)	36(5.2)	24(4.1)	15(4.7)	6.39e+35	—
	1.2	2023	—	—	—	—	—	—	—	—	—	—	—
013408.2+303851	01:34:08.296	1730	9.7(4.3)	<6.6	8.7(4.1)	—	—	—	7.0(3.1)	<5.0	6.3(2.2)	1.25e+35	—
	30:38:51.73	786	15.4(5.7)	<14.6	11.0 ^b (3.3)	—	—	—	7.1(2.6)	<11.0	8.3 ^b	1.27e+35	—
	1.1	2023	<4.6	<4.6	<4.6	—	—	—	<3.5	<3.5	<3.5	<6.30e+34	—
013408.4+304632	01:34:08.415	1730	26.1(6.5)	19.1(5.6)	<12.6	20.4(5.7)	2.4(2.9)	3.0(3.4)	20(4.9)	14(3.4)	<9.5	3.54e+35	—
	30:46:32.86	786	17.9(5.9)	16.8(5.7)	<9.3	—	—	—	17(5.4)	17(5.5)	<7.0	2.99e+35	—
	1.5	2023	15.9(5.5)	17.4(5.5)	<5.7	—	—	—	14(4.5)	15(4.5)	<4.3	2.57e+35	—
013408.5+303850	01:34:08.538	1730	8.0 ^b (2.8)	<6.0	<6.0	—	—	—	6.0 ^b	<4.5	<4.5	1.07e+35 ^b	—
	30:38:50.45	786	19.0 ^b (4.4)	<13.4	15.8(5.6)	—	—	—	14.3 ^b	<10.1	11(3.7)	2.56e+35 ^b	—
	1.1	2023	<4.6	<4.6	<4.6	—	—	—	<3.5	<3.5	<3.5	<6.30e+34	—
013409.7+303259	01:34:09.745	1730	29.5(6.8)	16.5(5.3)	8.0(4.1)	5.1(3.6)	14.4(5.0)	10.3(4.6)	23(5.2)	13(3.2)	6.2(2.3)	4.08e+35	—
	30:32:59.20	786	23.8(6.7)	18.8(5.9)	<18.0	5.6(4.0)	12.7(4.8)	4.6(4.1)	17(5.0)	14(4.3)	<13.5	3.07e+35	—
	1.8	2023	—	—	—	—	—	—	—	—	—	—	—
013409.8+305044	01:34:09.882	1730	—	—	—	—	—	—	—	—	—	—	—
	30:50:44.84	786	5.0 ^b (2.2)	<10.1	<8.5	—	—	—	3.8 ^b	<7.6	<6.4	6.80e+34 ^b	—
	1.6	2023	72.9(10.0)	45.5(7.9)	28.0(6.6)	2.7(3.2)	45.9(7.9)	25.1(6.5)	33(4.5)	21(3.6)	13(3.1)	5.95e+35	—
013409.9+303219	01:34:09.925	1730	—	—	—	—	—	—	—	—	—	—	—
	30:32:19.92	786	208.8(16.0)	213.7(16.0)	<9.3	207.2(15.6)	2.4(3.4)	<3.8	160(13)	170(12)	<7.0	2.93e+36	—
	1.3	2023	—	—	—	—	—	—	—	—	—	—	—
013409.9+305039	01:34:09.983	1730	—	—	—	—	—	—	—	—	—	—	—
	30:50:39.73	786	33.0(8.5)	23.4(7.0)	<25.6	6.3(4.6)	15.5(5.5)	11.4(6.0)	27(7.1)	19(5.7)	<19.2	4.78e+35	—
	1.5	2023	<9.1	<8.5	<6.0	—	—	—	<6.8	<6.4	<4.5	<1.22e+35	—
013410.3+305346	01:34:10.350	1730	—	—	—	—	—	—	—	—	—	—	—
	30:53:46.13	786	<6.6	<6.6	<4.6	—	—	—	<5.0	<5.0	<3.5	<9.00e+34	—
	2.4	2023	58.0(9.3)	38.0(7.5)	20.1(6.0)	12.9(5.0)	25.3(6.3)	20.1(6.2)	23(3.8)	15(3.0)	8.4(2.5)	4.20e+35	—
013410.5+303946	01:34:10.520	1730	100.2(11.1)	76.4(9.8)	24.4(6.1)	25.8(6.2)	51.9(8.3)	22.6(5.9)	72(7.9)	55(6.3)	17(3.6)	1.28e+36	—
	30:39:46.57	786	248.9(17.1)	194.1(15.2)	53.0(8.6)	96.3(11.0)	105.3(11.4)	47.7(8.3)	120(8.0)	83(6.5)	37(6.0)	2.09e+36	—
	1.0	2023	276.0(18.4)	183.0(14.9)	94.1(11.5)	49.9(8.5)	133.8(12.8)	93.9(11.4)	120(7.7)	77(6.2)	41(5.0)	2.09e+36	—
013410.6+304223	01:34:10.672	1730	75.5(9.8)	73.3(9.6)	<9.1	57.7(8.7)	15.7(5.1)	1.9(2.9)	56(7.3)	55(6.4)	<6.8	1.01e+36	—
	30:42:23.64	786	—	—	—	—	—	—	—	—	—	—	—
	1.0	2023	147.5(14.1)	145.8(13.5)	<14.6	105.0(11.5)	40.9(7.8)	1.8(5.0)	60(5.7)	59(5.4)	<11.0	1.07e+36	—
013410.7+305008	01:34:10.766	1730	—	—	—	—	—	—	—	—	—	—	—
	30:50:08.65	786	<4.6	<4.6	<4.6	—	—	—	<3.5	<3.5	<3.5	<6.30e+34	—
	1.4	2023	21.5(6.0)	<12.2	15.8(5.2)	1.5(2.7)	2.6(2.9)	17.7(5.4)	9.9(2.7)	<9.2	7.3(2.4)	1.77e+35	—
013411.8+304016	01:34:11.809	1730	5.0 ^b (2.2)	<6.6	3.8(3.2)	—	—	—	3.8 ^b	<5.0	2.7(1.4)	6.80e+34 ^b	—
	30:40:16.82	786	<7.5	<4.6	<7.5	—	—	—	<5.6	<3.5	<5.6	<1.00e+35	—
	1.1	2023	<6.0	<4.6	<6.0	—	—	—	<4.5	<3.5	<4.5	<8.10e+34	—

Table 3—Continued

Source CXO J	Coord./Unc. RA/Dec/["]	ObsId	Counts						Flux[10^{-7} cts/s/cm 2] ^a			L [erg/s] ^a 0.3–8.0
			0.3–8.0	0.3–2.0	2.0–8.0	0.3–1.0	1.0–2.1	2.1–8.0	0.3–8.0	0.3–2.0	2.0–8.0	
013412.1+304737	01:34:12.121	1730	—	—	—	—	—	—	—	—	—	—
	30:47:37.23	786	<6.6	<4.6	<6.6	—	—	—	<5.0	<3.5	<5.0	<9.00e+34
	1.2	2023	5.5(3.6)	<8.5	<10.0	—	—	—	2.1(1.4)	<6.4	<7.5	3.72e+34
013412.8+303554	01:34:12.860	1730	<22.8	7.3(4.0)	<12.2	—	—	—	<17.1	5.5(2.1)	<9.2	<3.06e+35
	30:35:54.57	786	<20.0	<14.4	<12.1	—	—	—	<15.0	<10.8	<9.1	<2.68e+35
	1.4	2023	—	—	—	—	—	—	—	—	—	—
013414.1+305352	01:34:14.180	1730	—	—	—	—	—	—	—	—	—	—
	30:53:52.49	786	<4.6	<4.6	<4.6	—	—	—	<3.5	<3.5	<3.5	<6.30e+34
	2.1	2023	27.4(7.6)	24.8(6.4)	<12.9	16.9(5.6)	8.5(4.4)	2.2(4.4)	11(3.0)	9.8(2.5)	<9.7	1.95e+35
013414.5+303250	01:34:14.506	1730	—	—	—	—	—	—	—	—	—	—
	30:32:50.02	786	13.0 ^b (3.6)	<9.3	11.8(5.1)	—	—	—	<9.8	<7.0	9.3(4.1)	<1.75e+35
	2.1	2023	—	—	—	—	—	—	—	—	—	—
013414.8+303412	01:34:14.806	1730	12.6(4.8)	6.0 ^b (2.5)	6.0 ^b (2.5)	—	—	—	9.9(3.7)	4.5 ^b	4.5 ^b	1.76e+35
	30:34:12.70	786	9.0 ^b (3.0)	7.0 ^b (2.7)	<7.5	—	—	—	6.8 ^b	5.3 ^b	<5.6	1.22e+35 ^b
	1.8	2023	—	—	—	—	—	—	—	—	—	—
013415.0+304748	01:34:15.073	1730	—	—	—	—	—	—	—	—	—	—
	30:47:48.67	786	<4.6	<4.6	<4.6	—	—	—	<3.5	<3.5	<3.5	<6.30e+34
	1.1	2023	11.2(4.7)	<9.1	8.2(4.1)	—	—	—	6.1(2.5)	<6.8	4.4(2.2)	1.10e+35
013416.3+305403	01:34:16.307	1730	—	—	—	—	—	—	—	—	—	—
	30:54:03.43	786	<6.6	<4.6	<6.6	—	—	—	<5.0	<3.5	<5.0	<9.00e+34
	2.0	2023	9.0(4.3)	<10.1	6.0 ^b (2.5)	—	—	—	3.6(1.7)	<7.6	4.5 ^b	6.36e+34
013416.3+305154	01:34:16.374	1730	—	—	—	—	—	—	—	—	—	—
	30:51:54.72	786	<8.5	<6.6	<6.6	—	—	—	<6.4	<5.0	<5.0	<1.15e+35
	1.3	2023	39.6(8.1)	41.7(7.9)	<9.8	29.7(6.7)	10.2(4.6)	<3.6	15(3.1)	16(3.0)	<7.4	2.69e+35
013416.6+304410	01:34:16.682	1730	<4.6	<4.6	<4.6	—	—	—	<3.5	<3.5	<3.5	<6.30e+34
	30:44:10.23	786	<6.6	<6.6	<4.6	—	—	—	<5.0	<5.0	<3.5	<9.00e+34
	1.2	2023	14.8(5.1)	8.7(4.1)	6.0 ^b (2.5)	—	—	—	5.7(2.0)	3.3(1.6)	4.5 ^b	1.02e+35
013416.7+305101	01:34:16.735	1730	—	—	—	—	—	—	—	—	—	—
	30:51:01.53	786	<10.2	<10.1	<6.6	—	—	—	<7.7	<7.5	<5.0	<1.38e+35
	1.2	2023	72.2(9.8)	42.0(7.6)	28.5(6.5)	8.1(4.1)	36.3(7.1)	27.5(6.5)	27(3.7)	16(2.9)	11(2.5)	4.88e+35
013417.0+303425	01:34:17.074	1730	24.1(6.3)	7.6(4.0)	11.6(4.7)	<1.9	12.5(4.7)	12.6(4.8)	18(4.7)	5.8(2.1)	9.0(2.8)	3.28e+35
	30:34:25.59	786	39.5(7.8)	33.6(7.9)	25.9(7.3)	5.2(3.8)	17.0(5.3)	16.6(5.6)	29(5.8)	24(5.8)	19(5.7)	5.16e+35
	1.9	2023	—	—	—	—	—	—	—	—	—	—
013417.1+304842	01:34:17.142	1730	—	—	—	—	—	—	—	—	—	—
	30:48:42.02	786	<6.6	<6.6	<4.6	—	—	—	<5.0	<5.0	<3.5	<9.00e+34
	1.1	2023	19.8(5.7)	6.0 ^b (2.5)	14.4(5.0)	—	—	—	7.3(2.1)	4.5 ^b	5.4(1.9)	1.31e+35
013417.4+304124	01:34:17.444	1730	<7.5	<8.5	<4.6	—	—	—	<5.6	<6.4	<3.5	<1.00e+35
	30:41:24.04	786	—	—	—	—	—	—	—	—	—	—
	1.4	2023	12.0 ^b (3.5)	13.8(5.1)	<6.5	—	—	—	9.0 ^b	5.5(2.0)	<4.9	1.61e+35 ^b
013419.1+304326	01:34:19.182	1730	<6.5	<6.0	<5.7	—	—	—	<4.9	<4.5	<4.3	8.80e+34
	30:43:26.17	786	<20.9	<7.5	8.8(4.4)	—	—	—	<15.7	<5.6	6.4(3.4)	<2.81e+35
	1.3	2023	<4.6	<4.6	<4.6	—	—	—	<3.5	<3.5	<3.5	<6.30e+34
013419.2+304942	01:34:19.294	1730	—	—	—	—	—	—	—	—	—	—
	30:49:42.07	786	<6.6	<6.6	<4.6	—	—	—	<5.0	<5.0	<3.5	<9.00e+34
	1.0	2023	47.3(8.1)	22.4(5.9)	24.7(6.2)	2.6(2.9)	21.7(5.8)	22.8(6.0)	17(3.0)	8.3(2.2)	9.2(2.3)	3.12e+35

Table 3—Continued

Source CXO J	Coord./Unc. RA/Dec/["]	ObsId	Counts						Flux[10^{-7} cts/s/cm 2] ^a			L [erg/s] ^a 0.3–8.0
			0.3–8.0	0.3–2.0	2.0–8.0	0.3–1.0	1.0–2.1	2.1–8.0	0.3–8.0	0.3–2.0	2.0–8.0	
013419.3+304239	01:34:19.300	1730	<4.6	<4.6	<4.6	—	—	—	<3.5	<3.5	<3.5	<6.30e+34
	30:42:39.02	786	<4.6	<4.6	<4.6	—	—	—	<3.5	<3.5	<3.5	<6.30e+34
	1.4	2023	9.0 ^b (3.0)	8.8(4.3)	<6.6	—	—	—	6.8 ^b	3.4(1.7)	<5.0	1.22e+35 ^b
013419.7+303719	01:34:19.783	1730	8.2(4.4)	7.4(4.0)	<8.3	—	—	—	6.3(3.4)	5.6(2.1)	<6.2	1.14e+35
	30:37:19.60	786	<12.2	<10.5	<8.3	—	—	—	<9.2	<7.9	<6.2	<1.65e+35
	1.6	2023	—	—	—	—	—	—	—	—	—	—
013419.8+304234	01:34:19.846	1730	<4.6	<4.6	<4.6	—	—	—	<3.5	<3.5	<3.5	<6.30e+34
	30:42:34.96	786	<4.6	<4.6	<4.6	—	—	—	<3.5	<3.5	<3.5	<6.30e+34
	1.4	2023	8.9(5.0)	7.0 ^b (2.7)	<10.8	—	—	—	3.4(1.9)	5.3 ^b	<8.1	6.12e+34
013420.9+305001	01:34:20.946	1730	—	—	—	—	—	—	—	—	—	—
	30:50:01.65	786	<8.5	<4.6	<8.5	—	—	—	<6.4	<3.5	<6.4	<1.15e+35
	1.0	2023	15.0(5.2)	9.4(4.3)	7.1(4.0)	—	—	—	5.5(1.9)	3.4(1.6)	2.6(1.5)	9.82e+34
013421.1+303928	01:34:21.174	1730	<6.0	<6.6	<4.6	—	—	—	<4.5	<5.0	<3.5	<8.10e+34
	30:39:28.57	786	—	—	—	—	—	—	—	—	—	—
	1.6	2023	17.2(6.0)	11.7(5.6)	<17.8	—	—	—	7.2(2.5)	4.9(2.3)	<13.4	1.29e+35
013421.2+304932	01:34:21.261	1730	—	—	—	—	—	—	—	—	—	—
	30:49:32.61	786	27.9(7.6)	11.0 ^b (3.3)	18.1(5.8)	2.3(3.6)	9.7(4.6)	15.8(6.0)	23(6.4)	8.3 ^b	16(5.1)	4.20e+35
	1.0	2023	119.0(12.0)	40.6(7.5)	78.1(9.9)	2.5(2.9)	41.6(7.5)	74.6(9.8)	44(4.4)	15(2.7)	29(3.7)	7.80e+35
013421.4+304448	01:34:21.427	1730	<6.6	<6.6	<4.6	—	—	—	<5.0	<5.0	<3.5	<9.00e+34
	30:44:48.30	786	6.0 ^b (2.5)	<8.5	<10.2	—	—	—	4.5 ^b	<6.4	<7.7	8.06e+34 ^b
	1.1	2023	6.4(4.0)	<12.2	<9.1	—	—	—	2.6(1.6)	<9.2	<6.8	4.62e+34
013421.9+304242	01:34:21.913	1730	<4.6	<4.6	<4.6	—	—	—	<3.5	<3.5	<3.5	<6.30e+34
	30:42:42.36	786	<8.5	<6.6	<6.6	—	—	—	<6.4	<5.0	<5.0	<1.15e+35
	1.3	2023	<10.1	2.9(2.9)	<4.6	—	—	—	<7.6	1.2(1.2)	<3.5	<1.36e+35
013423.5+305426	01:34:23.516	1730	—	—	—	—	—	—	—	—	—	—
	30:54:26.23	786	<4.6	<4.6	<4.6	—	—	—	<3.5	<3.5	<3.5	<6.30e+34
	1.7	2023	10.2(4.7)	19.1(5.8)	<11.1	—	—	—	4.5(2.0)	8.7(2.6)	<8.3	8.03e+34
013423.6+303833	01:34:23.678	1730	9.0 ^b (3.0)	8.2(4.1)	<7.5	—	—	—	6.8 ^b	6.3(2.3)	<5.6	1.22e+35 ^b
	30:38:33.10	786	—	—	—	—	—	—	—	—	—	—
	1.9	2023	—	—	—	—	—	—	—	—	—	—
013423.8+303847	01:34:23.851	1730	28.8(6.8)	19.7(5.8)	12.8(5.2)	4.1(3.4)	16.4(5.2)	9.2(4.4)	23(5.3)	15(3.6)	10(3.2)	4.05e+35
	30:38:47.12	786	—	—	—	—	—	—	—	—	—	—
	1.9	2023	21.0(6.9)	16.3(6.1)	7.3(5.0)	2.7(3.2)	16.9(5.3)	8.6(4.6)	25(6.1)	16(4.6)	14(5.6)	4.46e+35
013424.2+304406	01:34:24.225	1730	<4.6	<4.6	<4.6	—	—	—	<3.5	<3.5	<3.5	<6.30e+34
	30:44:06.01	786	<6.6	<4.6	<6.6	—	—	—	<5.0	<3.5	<5.0	<9.00e+34
	1.1	2023	<10.1	2.9(2.9)	<4.6	—	—	—	<7.6	1.1(1.1)	<3.5	<1.36e+35
013424.4+305104	01:34:24.455	1730	—	—	—	—	—	—	—	—	—	—
	30:51:04.95	786	<4.6	<4.6	<4.6	—	—	—	<3.5	<3.5	<3.5	<6.30e+34
	1.0	2023	6.4(3.8)	<10.2	<10.1	—	—	—	2.4(1.4)	<7.7	<7.6	4.21e+34
013424.5+304306	01:34:24.524	1730	9.6(4.4)	<16.5	<12.2	—	—	—	7.3(3.4)	<12.4	<9.2	1.30e+35
	30:43:06.39	786	25.8(7.0)	22.2(6.3)	<18.2	4.9(3.8)	15.0(5.2)	4.3(4.4)	19(5.3)	16(4.7)	<13.7	3.33e+35
	1.2	2023	52.8(8.5)	27.1(6.4)	26.3(6.4)	5.2(3.6)	22.4(5.9)	25.0(6.3)	20(3.3)	10(2.4)	10(2.5)	3.61e+35
013424.6+304428	01:34:24.628	1730	<6.8	<7.5	<5.2	—	—	—	<5.1	<5.6	<3.9	9.10e+34
	30:44:28.85	786	35.4(7.8)	18.5(5.8)	19.5(6.1)	6.8(4.1)	10.9(4.7)	16.1(5.9)	26(6.0)	14(4.4)	15(4.8)	4.70e+35
	1.0	2023	<9.1	<10.1	<4.6	—	—	—	<6.8	<7.6	<3.5	<1.22e+35

Table 3—Continued

Source CXO J	Coord./Unc. RA/Dec/["]	ObsId	Counts						Flux[10^{-7} cts/s/cm 2] ^a			L [erg/s] ^a 0.3–8.0
			0.3–8.0	0.3–2.0	2.0–8.0	0.3–1.0	1.0–2.1	2.1–8.0	0.3–8.0	0.3–2.0	2.0–8.0	
013424.7+303913	01:34:24.785	1730	<7.5	<7.4	<6.6	—	—	—	<5.6	<5.6	<5.0	<1.00e+35
	30:39:13.01	786	—	—	—	—	—	—	—	—	—	—
	2.0	2023	16.0(6.7)	<15.5	11.0 ^b (3.3)	—	—	—	6.8(2.7)	<11.6	<8.3	1.21e+35
013425.3+304157	01:34:25.368	1730	<20.3	<10.8	<16.5	—	—	—	<15.2	<8.1	<12.4	<2.72e+35
	30:41:57.82	786	44.9(8.3)	33.0(7.1)	15.8(5.6)	11.4(4.7)	19.4(5.7)	12.7(5.3)	33(6.2)	24(5.3)	12(4.3)	5.91e+35
	1.4	2023	26.7(7.0)	18.3(5.6)	<16.5	3.2(3.4)	18.5(5.6)	5.1(4.3)	11(2.9)	7.6(2.3)	<12.4	1.97e+35
013425.4+302821	01:34:25.481	1730	—	—	—	—	—	—	—	—	—	—
	30:28:21.70	786	112.7(14.5)	83.6(11.2)	29.0 ^b (5.4)	32.0(8.3)	52.7(9.0)	31.7(9.3)	100(13)	72(9.6)	<21.8	1.81e+36
	2.4	2023	—	—	—	—	—	—	—	—	—	—
013425.5+305514	01:34:25.501	1730	—	—	—	—	—	—	—	—	—	—
	30:55:14.88	786	1774.2(44.4)	1332.9(38.2)	432.9(23.2)	366.0(20.8)	1003.4(32.9)	431.6(22.9)	2000(49)	1500(41)	530(28)	3.55e+37
	0.7	2023	4404.5(67.5)	3283.3(58.4)	1380.7(38.4)	788.0(29.1)	2391.4(49.9)	1226.3(36.1)	2000(30)	1600(28)	680(19)	3.53e+37
013425.8+304636	01:34:25.875	1730	<4.6	<4.6	<4.6	—	—	—	<3.5	<3.5	<3.5	<6.30e+34
	30:46:36.73	786	<6.6	<4.6	<6.6	—	—	—	<5.0	<3.5	<5.0	<9.00e+34
	1.0	2023	<11.8	<4.6	3.7(3.2)	—	—	—	<8.9	<3.5	1.4(1.2)	<1.59e+35
013426.5+304446	01:34:26.575	1730	36.2(7.7)	22.8(6.2)	14.0 ^b (3.7)	8.6(4.3)	13.6(5.0)	14.3(5.4)	31(6.5)	19(4.2)	10.5 ^b	5.50e+35
	30:44:46.97	786	42.5(8.8)	28.4(7.1)	16.0 ^b (4.0)	4.2(4.0)	23.3(6.3)	13.0(6.1)	33(7.0)	22(5.6)	12.0 ^b	5.82e+35
	1.0	2023	91.2(10.7)	67.0(9.3)	23.9(6.1)	18.3(5.4)	49.4(8.1)	23.2(6.1)	34(4.0)	25(3.5)	9.0(2.3)	6.07e+35
013426.6+303737	01:34:26.608	1730	19.9(5.9)	16.8(5.3)	<11.1	—	—	—	15(4.5)	13(3.2)	<8.3	2.75e+35
	30:37:37.70	786	—	—	—	—	—	—	—	—	—	—
	2.3	2023	—	—	—	—	—	—	—	—	—	—
013426.7+304811	01:34:26.799	1730	—	—	—	—	—	—	—	—	—	—
	30:48:11.93	786	<4.6	<4.6	<4.6	—	—	—	<3.5	<3.5	<3.5	<6.30e+34
	1.0	2023	38.2(7.4)	18.6(5.4)	13.6(4.8)	2.6(2.9)	20.7(5.7)	14.8(5.1)	14(2.8)	7.0(2.1)	5.2(1.8)	2.57e+35
013427.0+304314	01:34:27.062	1730	27.7(6.7)	20.5(5.9)	9.0 ^b (3.0)	2.4(2.9)	16.4(5.2)	9.9(4.6)	25(5.9)	18(4.1)	6.8 ^b	4.43e+35
	30:43:14.47	786	62.0(9.7)	35.1(7.5)	25.1(6.7)	8.3(4.4)	28.4(6.6)	23.3(6.7)	46(7.4)	26(5.7)	19(5.3)	8.28e+35
	1.0	2023	107.9(11.6)	77.8(9.9)	30.5(6.7)	19.3(5.6)	59.4(8.8)	29.0(6.6)	41(4.4)	30(3.8)	12(2.6)	7.33e+35
013427.2+304421	01:34:27.277	1730	<10.1	<10.1	<4.6	—	—	—	<7.6	<7.6	<3.5	<1.36e+35
	30:44:21.86	786	<6.6	<6.6	<4.6	—	—	—	<5.0	<5.0	<3.5	<9.00e+34
	1.0	2023	10.1(4.4)	7.6(4.0)	<9.1	—	—	—	3.7(1.7)	2.8(1.5)	<6.8	6.70e+34
013428.1+303246	01:34:28.179	1730	—	—	—	—	—	—	—	—	—	—
	30:32:46.51	786	59.2(10.4)	42.0 ^b (6.5)	18.0 ^b (4.2)	13.7(5.8)	28.5(6.8)	17.3(6.8)	50(8.7)	31.5 ^b	13.5 ^b	8.90e+35
	3.6	2023	—	—	—	—	—	—	—	—	—	—
013429.0+304249	01:34:29.016	1730	<7.5	<8.5	<4.6	—	—	—	<5.6	<6.4	<3.5	<1.00e+35
	30:42:49.07	786	<10.1	<8.5	<6.6	—	—	—	<7.6	<6.4	<5.0	<1.36e+35
	1.2	2023	11.3(4.6)	7.7(4.0)	<10.2	—	—	—	4.3(1.7)	2.9(1.5)	<7.7	7.67e+34
013429.1+304212	01:34:29.135	1730	16.2(5.9)	9.0 ^b (3.0)	<17.8	—	—	—	13(4.5)	6.8 ^b	<13.4	2.28e+35
	30:42:12.44	786	<19.6	7.0 ^b (2.7)	<9.3	—	—	—	<14.7	5.3 ^b	<7.0	<2.63e+35
	1.2	2023	19.6(5.8)	18.7(5.6)	<12.2	—	—	—	7.5(2.2)	7.2(2.1)	<9.2	1.35e+35
013429.7+305026	01:34:29.742	1730	—	—	—	—	—	—	—	—	—	—
	30:50:26.16	786	<10.2	<6.6	<10.1	—	—	—	<7.7	<5.0	<7.6	<1.38e+35
	1.0	2023	93.7(10.8)	57.5(8.7)	34.9(7.1)	19.7(5.6)	40.7(7.5)	33.1(6.9)	34(3.9)	21(3.1)	13(2.5)	6.03e+35
013429.9+304236	01:34:29.917	1730	<4.6	<4.6	<4.6	—	—	—	<3.5	<3.5	<3.5	<6.30e+34
	30:42:36.39	786	<4.6	<4.6	<4.6	—	—	—	<3.5	<3.5	<3.5	<6.30e+34
	1.2	2023	6.0 ^b (2.5)	4.5(3.4)	<7.5	—	—	—	4.5 ^b	1.7(1.3)	<5.6	8.06e+34 ^b

Table 3—Continued

Source CXO J	Coord./Unc. RA/Dec/["]	ObsId	Counts						Flux[10 ⁻⁷ cts/s/cm ²] ^a			L [erg/s] ^a 0.3–8.0
			0.3–8.0	0.3–2.0	2.0–8.0	0.3–1.0	1.0–2.1	2.1–8.0	0.3–8.0	0.3–2.0	2.0–8.0	
013429.9+305106	01:34:29.956	1730	—	—	—	—	—	—	—	—	—	—
	30:51:06.87	786	<8.5	<8.5	<4.6	—	—	—	<6.4	<6.4	<3.5	<1.15e+35
	1.0	2023	22.4(5.9)	5.7(3.6)	16.1(5.2)	<1.9	10.9(4.4)	11.6(4.6)	8.1(2.1)	2.1(1.3)	5.8(1.9)	1.46e+35
013430.4+305041	01:34:30.491	1730	—	—	—	—	—	—	—	—	—	—
	30:50:41.78	786	<4.6	<4.6	<4.6	—	—	—	<3.5	<3.5	<3.5	<6.30e+34
	1.0	2023	12.0(4.7)	2.7(2.9)	<13.8	—	—	—	4.3(1.7)	0.98(1.1)	<10.4	7.68e+34
013430.9+304510	01:34:30.904	1730	—	—	—	—	—	—	—	—	—	—
	30:45:10.0	786	<4.6	<4.6	<4.6	—	—	—	<3.5	<3.5	<3.5	<6.30e+34
	1.0	2023	19.2(5.7)	11.5(4.6)	9.3(4.3)	—	—	—	7.4(2.2)	4.4(1.8)	3.6(1.7)	1.32e+35
013432.0+303455	01:34:32.020	1730	102.7(11.9)	28.4(6.7)	67.9(9.6)	2.4(3.6)	29.6(6.7)	73.2(10.0)	85(9.7)	24(4.6)	57(7.1)	1.52e+36
	30:34:55.00	786	—	—	—	—	—	—	—	—	—	—
	1.8	2023	—	—	—	—	—	—	—	—	—	—
013432.1+305158	01:34:32.148	1730	—	—	—	—	—	—	—	—	—	—
	30:51:58.81	786	<6.6	<6.6	<4.6	—	—	—	<5.0	<5.0	<3.5	<9.00e+34
	1.0	2023	68.5(9.5)	53.2(8.4)	13.4(4.8)	18.8(5.4)	38.9(7.3)	12.5(4.7)	93(13)	68(11)	20(7.0)	1.66e+36
013432.2+304958	01:34:32.238	1730	—	—	—	—	—	—	—	—	—	—
	30:49:58.73	786	<6.6	<4.6	<6.6	—	—	—	<5.0	<3.5	<5.0	<9.00e+34
	1.0	2023	6.5(3.8)	3.7(3.2)	<8.5	—	—	—	2.3(1.3)	1.3(1.1)	<6.4	4.11e+34
013432.2+303159	01:34:32.277	1730	—	—	—	—	—	—	—	—	—	—
	30:31:59.23	786	27.0 ^b (5.2)	18.0(6.3)	<22.1	—	—	—	<20.3	15(5.1)	<16.6	3.64e+35
	4.6	2023	—	—	—	—	—	—	—	—	—	—
013432.5+303928	01:34:32.523	1730	<18.2	<6.5	8.0 ^b (2.8)	—	—	—	<13.7	<4.9	6.0 ^b	<2.45e+35
	30:39:28.22	786	13.0 ^b (3.6)	<8.3	12.0(5.0)	—	—	—	9.8 ^b	<6.2	9.2(3.9)	1.75e+35 ^b
	2.0	2023	<7.5	<4.6	<7.5	—	—	—	<5.6	<3.5	<5.6	<1.00e+35
013432.5+305035	01:34:32.595	1730	—	—	—	—	—	—	—	—	—	—
	30:50:35.41	786	<6.6	<4.6	<6.6	—	—	—	<5.0	<3.5	<5.0	<9.00e+34
	1.0	2023	35.8(7.1)	13.7(4.8)	21.4(5.8)	0.7(2.3)	13.8(4.8)	21.2(5.8)	15(3.0)	6.4(2.3)	8.8(2.4)	2.67e+35
013432.7+303436	01:34:32.704	1730	54.6(9.6)	33.7(7.3)	18.0 ^b (4.2)	10.2(4.9)	29.4(6.7)	18.8(6.2)	51(8.3)	29(5.2)	13.5 ^b	9.05e+35
	30:34:36.04	786	<4.8	<5.1	<4.6	—	—	—	<3.6	<3.8	<3.5	6.45e+34
	3.7	2023	—	—	—	—	—	—	—	—	—	—
013433.0+304638	01:34:33.021	1730	—	—	—	—	—	—	—	—	—	—
	30:46:38.00	786	<10.2	<10.2	<4.6	—	—	—	<7.7	<7.7	<3.5	<1.38e+35
	1.0	2023	33.6(7.0)	36.0(7.1)	<7.5	20.6(5.7)	11.7(4.6)	1.1(2.7)	12(2.5)	13(2.6)	<5.6	2.16e+35
013433.6+305500	01:34:33.614	1730	—	—	—	—	—	—	—	—	—	—
	30:55:00.39	786	—	—	—	—	—	—	—	—	—	—
	1.7	2023	25.5(6.6)	<12.6	22.0(6.1)	<2.3	4.9(3.6)	20.2(6.0)	10(2.7)	<9.5	8.7(2.4)	1.79e+35
013433.7+304701	01:34:33.763	1730	—	—	—	—	—	—	—	—	—	—
	30:47:01.92	786	421.1(27.4)	353.7(22.4)	67.4(16.6)	221.0(16.9)	103.2(12.5)	56.9(13.1)	430(27)	340(22)	87(18)	7.66e+36
	1.0	2023	819.6(36.4)	781.9(31.9)	37.6(18.4)	467.7(24.6)	265.9(19.4)	101.0(19.1)	280(14)	280(12)	3.0(7.7)	5.00e+36
013433.9+305021	01:34:33.929	1730	—	—	—	—	—	—	—	—	—	—
	30:50:21.42	786	3.1(3.4)	<7.5	<9.1	—	—	—	2.6(2.9)	<5.6	<6.8	4.56e+34
	1.0	2023	<4.6	<4.6	<4.6	—	—	—	<3.5	<3.5	<3.5	<6.30e+34
013434.1+305136	01:34:34.195	1730	—	—	—	—	—	—	—	—	—	—
	30:51:36.00	786	4.6(4.3)	<8.3	<14.6	—	—	—	4.0(3.7)	<6.2	<11.0	7.10e+34
	1.0	2023	11.0(4.6)	5.0 ^b (2.2)	4.5(3.4)	—	—	—	4.0(1.7)	3.8 ^b	1.6(1.3)	7.23e+34

Table 3—Continued

Source CXO J	Coord./Unc. RA/Dec/["]	ObsId	Counts						Flux[10^{-7} cts/s/cm 2] ^a			L [erg/s] ^a 0.3–8.0
			0.3–8.0	0.3–2.0	2.0–8.0	0.3–1.0	1.0–2.1	2.1–8.0	0.3–8.0	0.3–2.0	2.0–8.0	
013434.2+305254	01:34:34.217	1730	—	—	—	—	—	—	—	—	—	—
	30:52:54.82	786	3.4(3.4)	<9.1	<7.5	—	—	—	5.6(4.7)	<6.8	<5.6	1.01e+35
	1.1	2023	<4.6	<4.6	<4.6	—	—	—	<3.5	<3.5	<3.5	<6.30e+34
013435.0+304439	01:34:35.032	1730	—	—	—	—	—	—	—	—	—	—
	30:44:39.16	786	<10.2	<6.6	<10.1	—	—	—	<7.7	<5.0	<7.6	<1.38e+35
	1.0	2023	47.3(8.1)	11.6(4.6)	37.0(7.2)	<1.9	10.7(4.4)	36.9(7.2)	17(3.0)	4.3(1.7)	14(2.7)	3.11e+35
013435.0+304711	01:34:35.090	1730	—	—	—	—	—	—	—	—	—	—
	30:47:11.52	786	<8.5	<8.5	<4.6	—	—	—	<6.4	<6.4	<3.5	<1.15e+35
	1.0	2023	12.0 ^b (3.5)	<10.1	9.6(4.3)	—	—	—	9.0 ^b	<7.6	3.5(1.6)	1.61e+35 ^b
013435.1+305034	01:34:35.107	1730	—	—	—	—	—	—	—	—	—	—
	30:50:34.33	786	7.3(5.0)	<10.2	<18.0	—	—	—	6.7(4.4)	<7.7	<13.5	1.20e+35
	1.0	2023	<6.0	<4.6	<6.0	—	—	—	<4.5	<3.5	<4.5	<8.10e+34
013435.1+305646	01:34:35.152	1730	—	—	—	—	—	—	—	—	—	—
	30:56:46.29	786	—	—	—	—	—	—	—	—	—	—
	1.5	2023	159.1(14.9)	72.1(10.0)	76.7(10.3)	0.5(3.8)	76.7(10.2)	81.5(11.2)	68(6.4)	31(4.3)	33(4.5)	1.21e+36
013435.3+305208	01:34:35.372	1730	—	—	—	—	—	—	—	—	—	—
	30:52:08.81	786	<6.6	<6.6	<4.6	—	—	—	<5.0	<5.0	<3.5	<9.00e+34
	1.0	2023	<12.2	3.8(3.2)	<6.6	—	—	—	<9.2	1.4(1.2)	<5.0	<1.65e+35
013435.3+304946	01:34:35.389	1730	—	—	—	—	—	—	—	—	—	—
	30:49:46.10	786	<10.1	<8.5	<6.6	—	—	—	<7.6	<6.4	<5.0	<1.36e+35
	1.0	2023	5.6(3.6)	3.5(3.2)	<8.5	—	—	—	6.1(3.8)	4.1(3.4)	<6.4	1.09e+35
013436.0+303450	01:34:36.096	1730	63.7(10.7)	37.3(7.7)	21.6(7.1)	3.1(4.2)	42.9(7.9)	23.8(7.0)	61(9.3)	32(5.5)	21(5.2)	1.08e+36
	30:34:50.24	786	—	—	—	—	—	—	—	—	—	—
	4.3	2023	—	—	—	—	—	—	—	—	—	—
013436.4+304713	01:34:36.487	1730	—	—	—	—	—	—	—	—	—	—
	30:47:13.99	786	67.0 ^b (8.2)	20.0 ^b (4.5)	47.0(9.0)	—	—	—	50.3 ^b	15.0 ^b	43(8.2)	9.01e+35 ^b
	1.0	2023	65.3(9.2)	<10.1	65.1(9.2)	0.8(2.3)	1.9(2.7)	62.6(9.0)	23(3.3)	<7.6	24(3.3)	4.20e+35
013436.6+304314	01:34:36.647	1730	—	—	—	—	—	—	—	—	—	—
	30:43:14.67	786	<8.5	<8.5	<4.6	—	—	—	<6.4	<6.4	<3.5	<1.15e+35
	1.1	2023	8.6(4.3)	<7.5	7.0 ^b (2.7)	—	—	—	3.2(1.6)	<5.6	5.3 ^b	5.72e+34
013437.4+305033	01:34:37.437	1730	—	—	—	—	—	—	—	—	—	—
	30:50:33.77	786	7.4(4.6)	<9.7	<14.4	—	—	—	6.5(4.0)	<7.3	<10.8	1.16e+35
	1.0	2023	<4.6	<4.6	<4.6	—	—	—	<3.5	<3.5	<3.5	<6.30e+34
013438.8+304538	01:34:38.831	1730	—	—	—	—	—	—	—	—	—	—
	30:45:38.78	786	108.9(12.6)	96.6(11.7)	29.0 ^b (5.4)	30.9(7.1)	50.1(8.5)	26.6(7.6)	89(10)	78(9.5)	21.8 ^b	1.59e+36
	1.0	2023	213.3(15.7)	156.0(13.6)	58.5(8.7)	48.6(8.1)	108.7(11.5)	55.9(8.6)	77(5.7)	56(4.9)	21(3.2)	1.38e+36
013438.8+305504	01:34:38.833	1730	—	—	—	—	—	—	—	—	—	—
	30:55:04.23	786	—	—	—	—	—	—	—	—	—	—
	0.7	2023	2429.1(50.5)	1741.3(42.8)	692.4(27.5)	508.6(23.6)	1270.8(36.7)	648.6(26.7)	1000(21)	710(18)	290(11)	1.78e+37
013438.9+305014	01:34:38.996	1730	—	—	—	—	—	—	—	—	—	—
	30:50:14.38	786	6.6(4.7)	<7.5	<18.0	—	—	—	5.6(4.0)	<5.6	<13.5	1.00e+35
	1.0	2023	<6.0	<4.6	<6.0	—	—	—	<4.5	<3.5	<4.5	<8.10e+34
013439.0+304115	01:34:39.028	1730	—	—	—	—	—	—	—	—	—	—
	30:41:15.12	786	<8.5	<8.5	<4.6	—	—	—	<6.4	<6.4	<3.5	<1.15e+35
	1.4	2023	24.3(7.1)	<18.0	17.0 ^b (4.1)	<2.7	9.8(4.6)	15.0(5.8)	9.4(2.8)	<13.5	12.8 ^b	1.69e+35

Table 3—Continued

Source CXO J	Coord./Unc. RA/Dec/["]	ObsId	Counts						Flux[10^{-7} cts/s/cm 2] ^a			L [erg/s] ^a 0.3–8.0
			0.3–8.0	0.3–2.0	2.0–8.0	0.3–1.0	1.0–2.1	2.1–8.0	0.3–8.0	0.3–2.0	2.0–8.0	
013439.8+305143	01:34:39.875	1730	—	—	—	—	—	—	—	—	—	—
	30:51:43.40	786	—	—	—	—	—	—	—	—	—	—
	1.0	2023	126.4(12.4)	85.0(10.3)	45.3(7.9)	21.4(5.8)	62.5(9.0)	42.0(7.7)	47(4.6)	32(3.9)	17(2.9)	8.39e+35
013440.8+304409	01:34:40.846	1730	—	—	—	—	—	—	—	—	—	—
	30:44:09.58	786	<10.1	<8.5	<6.6	—	—	—	<7.6	<6.4	<5.0	<1.36e+35
	1.0	2023	27.8±6.5	18.5(5.4)	9.0 ^b (3.0)	6.7(3.8)	11.8(4.6)	9.3(4.3)	10(2.4)	6.8(2.0)	6.8 ^b	1.84e+35
013441.0+304325	01:34:41.070	1730	—	—	—	—	—	—	—	—	—	—
	30:43:25.84	786	<8.5	<8.5	<4.6	—	—	—	<6.4	<6.4	<3.5	<1.15e+35
	1.1	2023	40.7(7.9)	51.5(8.7)	<12.1	30.5(6.7)	6.8(4.0)	3.0(3.8)	15(3.0)	19(3.2)	<9.1	2.70e+35
013441.2+304330	01:34:41.207	1730	—	—	—	—	—	—	—	—	—	—
	30:43:30.37	786	20.4(6.6)	24.7(6.9)	<10.2	15.2(5.2)	2.3(3.2)	3.4(4.1)	18(5.7)	21(5.9)	<7.7	3.18e+35
	1.1	2023	7.0 ^b (2.7)	<15.5	<7.5	—	—	—	5.3 ^b	<11.6	<5.6	9.51e+34 ^b
013441.6+305033	01:34:41.653	1730	—	—	—	—	—	—	—	—	—	—
	30:50:33.89	786	10.1(5.4)	<16.0	<13.8	—	—	—	13(5.9)	<12.0	<10.4	2.33e+35
	1.0	2023	<7.5	<8.5	<4.6	—	—	—	<5.6	<6.4	<3.5	<1.00e+35
013442.0+305229	01:34:42.066	1730	—	—	—	—	—	—	—	—	—	—
	30:52:29.09	786	—	—	—	—	—	—	—	—	—	—
	1.1	2023	60.5(9.0)	44.7(7.8)	17.0(5.3)	6.5(3.8)	36.5(7.1)	17.2(5.4)	24(3.6)	18(3.1)	6.7(2.1)	4.30e+35
013442.5+305249	01:34:42.515	1730	—	—	—	—	—	—	—	—	—	—
	30:52:49.33	786	—	—	—	—	—	—	—	—	—	—
	1.2	2023	68.2(9.5)	33.0 ^b (5.7)	35.3(7.1)	5.2(3.6)	27.2(6.4)	35.2(7.2)	26(3.6)	24.8 ^b	13(2.7)	4.61e+35
013442.6+304927	01:34:42.669	1730	—	—	—	—	—	—	—	—	—	—
	30:49:27.39	786	<6.6	<4.6	<6.6	—	—	—	<5.0	<3.5	<5.0	<9.00e+34
	1.0	2023	7.2(4.0)	<10.1	4.6(3.4)	—	—	—	2.6(1.4)	<7.6	1.6(1.2)	4.57e+34
013442.7+305050	01:34:42.793	1730	—	—	—	—	—	—	—	—	—	—
	30:50:50.44	786	—	—	—	—	—	—	—	—	—	—
	1.0	2023	9.0 ^b (3.0)	<6.6	8.2(4.1)	—	—	—	<6.8	<5.0	2.9(1.5)	<1.22e+35
013442.8+304505	01:34:42.840	1730	—	—	—	—	—	—	—	—	—	—
	30:45:05.86	786	50.4(9.5)	31.7(7.3)	18.0 ^b (4.2)	10.7(5.0)	20.9(6.1)	18.0(6.7)	41(7.9)	26(6.0)	13.5 ^b	7.39e+35
	1.0	2023	77.9(9.9)	56.6(8.6)	21.1(5.8)	18.8(5.4)	37.8(7.2)	21.2(5.8)	28(3.6)	21(3.1)	7.6(2.1)	5.06e+35
013443.1+304948	01:34:43.136	1730	—	—	—	—	—	—	—	—	—	—
	30:49:48.61	786	<4.6	<4.6	<4.6	—	—	—	<3.5	<3.5	<3.5	<6.30e+34
	1.0	2023	25.4(6.3)	6.7(3.8)	8.7(4.1)	1.6(2.7)	15.6(5.1)	7.7(4.1)	9.1(2.3)	2.4(1.4)	3.1(1.5)	1.62e+35
013444.3+304702	01:34:44.363	1730	—	—	—	—	—	—	—	—	—	—
	30:47:02.90	786	<4.6	<4.6	<4.6	—	—	—	<3.5	<3.5	<3.5	<6.30e+34
	1.0	2023	26.9(6.4)	16.8(5.2)	10.7(4.4)	1.8(2.7)	15.8(5.1)	9.2(4.3)	9.6(2.3)	6.0(1.9)	3.8(1.6)	1.71e+35
013444.5+304922	01:34:44.561	1730	—	—	—	—	—	—	—	—	—	—
	30:49:22.42	786	81.7(12.1)	51.3(9.1)	29.0 ^b (5.4)	26.2(7.0)	30.6(7.1)	31.7(8.2)	88(12)	54(9.1)	21.8 ^b	1.57e+36
	1.0	2023	152.2(13.4)	138.3(12.8)	14.7(5.0)	68.6(9.4)	71.6(9.5)	11.6(4.7)	55(4.9)	50(4.6)	5.2(1.8)	9.82e+35
013444.6+305535	01:34:44.637	1730	—	—	—	—	—	—	—	—	—	—
	30:55:35.46	786	—	—	—	—	—	—	—	—	—	—
	1.3	2023	314.7(19.2)	202.4(15.5)	129.6(12.8)	19.3(5.8)	173.4(14.3)	121.9(12.5)	140(8.3)	87(6.7)	56(5.6)	2.43e+36
013445.8+305222	01:34:45.853	1730	—	—	—	—	—	—	—	—	—	—
	30:52:22.43	786	—	—	—	—	—	—	—	—	—	—
	1.2	2023	10.5(4.6)	<7.5	7.4(4.0)	—	—	—	3.9(1.7)	<5.6	2.8(1.5)	6.95e+34

Table 3—Continued

Source CXO J	Coord./Unc. RA/Dec/["]	ObsId	Counts						Flux[10^{-7} cts/s/cm 2] ^a			L [erg/s] ^a 0.3–8.0
			0.3–8.0	0.3–2.0	2.0–8.0	0.3–1.0	1.0–2.1	2.1–8.0	0.3–8.0	0.3–2.0	2.0–8.0	
013446.7+304449	01:34:46.778	1730	—	—	—	—	—	—	—	—	—	—
	30:44:49.01	786	<8.5	<6.6	<6.6	—	—	—	<6.4	<5.0	<5.0	<1.15e+35
	1.0	2023	52.7(8.4)	46.1(7.9)	12.5(4.8)	10.8(4.4)	30.8(6.6)	11.1(4.6)	21(3.3)	18(3.0)	4.8(1.9)	3.68e+35
013447.4+304957	01:34:47.471	1730	—	—	—	—	—	—	—	—	—	—
	30:49:57.53	786	—	—	—	—	—	—	—	—	—	—
	1.0	2023	12.4(4.8)	5.7(3.6)	6.6(3.8)	—	—	—	4.4(1.8)	2.1(1.3)	2.4(1.4)	7.95e+34
013447.4+303958	01:34:47.488	1730	—	—	—	—	—	—	—	—	—	—
	30:39:58.44	786	21.1(7.3)	16.3(6.2)	<17.2	7.2(4.4)	8.4(4.6)	4.4(5.1)	17(6.1)	13(5.1)	<12.9	3.01e+35
	2.1	2023	—	—	—	—	—	—	—	—	—	—
013448.6+304706	01:34:48.629	1730	—	—	—	—	—	—	—	—	—	—
	30:47:06.55	786	<8.5	<4.6	<8.5	—	—	—	<6.4	<3.5	<6.4	<1.15e+35
	1.0	2023	7.3(4.0)	<8.5	5.6(3.6)	—	—	—	2.8(1.5)	<6.4	2.1(1.4)	4.98e+34
013449.0+304446	01:34:49.043	1730	—	—	—	—	—	—	—	—	—	—
	30:44:46.44	786	<8.5	<8.5	<4.6	—	—	—	<6.4	<6.4	<3.5	<1.15e+35
	1.1	2023	92.2(10.8)	51.1(8.3)	39.6(7.5)	15.3(5.1)	39.3(7.4)	37.2(7.4)	34(4.0)	19(3.0)	14(2.7)	6.05e+35
013449.3+304808	01:34:49.314	1730	—	—	—	—	—	—	—	—	—	—
	30:48:08.96	786	<4.6	<4.6	<4.6	—	—	—	<3.5	<3.5	<3.5	<6.30e+34
	1.0	2023	7.3(4.0)	7.8(4.0)	<4.6	—	—	—	2.8(1.5)	3.0(1.5)	<3.5	5.03e+34
013449.5+305011	01:34:49.516	1730	—	—	—	—	—	—	—	—	—	—
	30:50:11.93	786	—	—	—	—	—	—	—	—	—	—
	1.1	2023	9.1(4.3)	5.8(3.6)	<9.1	—	—	—	3.3(1.6)	2.1(1.3)	<6.8	5.94e+34
013451.1+304356	01:34:51.128	1730	—	—	—	—	—	—	—	—	—	—
	30:43:56.76	786	<4.6	<4.6	<4.6	—	—	—	<3.5	<3.5	<3.5	<6.30e+34
	1.2	2023	80.4(10.2)	63.3(9.1)	17.1(5.4)	7.3(4.0)	58.3(8.7)	14.5(5.2)	30(3.8)	24(3.4)	6.3(2.0)	5.37e+35
013451.8+304523	01:34:51.849	1730	—	—	—	—	—	—	—	—	—	—
	30:45:23.06	786	8.8(4.6)	<12.2	<15.7	—	—	—	7.7(4.0)	<9.2	<11.8	1.37e+35
	1.1	2023	<7.5	<8.5	<4.6	—	—	—	<5.6	<6.4	<3.5	<1.00e+35
013451.9+304615	01:34:51.938	1730	—	—	—	—	—	—	—	—	—	—
	30:46:15.84	786	137.5(15.6)	77.6(11.1)	57.0 ^b (7.6)	24.5(7.4)	60.1(9.7)	55.0(11.1)	120(14)	6.7(9.6)	42.8 ^b	2.18e+36
	1.0	2023	121.3(12.2)	85.2(10.3)	35.9(7.1)	25.5(6.2)	59.5(8.8)	36.2(7.2)	48(4.8)	34(4.1)	14(2.8)	8.56e+35
013452.2+305309	01:34:52.289	1730	—	—	—	—	—	—	—	—	—	—
	30:53:09.01	786	—	—	—	—	—	—	—	—	—	—
	1.6	2023	29.7(7.2)	25.4(6.3)	6.0 ^b (2.5)	5.6(3.8)	19.6(5.7)	4.2(4.1)	12(3.0)	11(2.6)	4.5 ^b	2.21e+35
013452.3+305037	01:34:52.386	1730	—	—	—	—	—	—	—	—	—	—
	30:50:37.72	786	—	—	—	—	—	—	—	—	—	—
	1.2	2023	17.4(5.4)	<13.8	11.8(4.7)	—	—	—	7.1(2.2)	<10.4	4.8(1.9)	1.28e+35
013452.5+304241	01:34:52.595	1730	—	—	—	—	—	—	—	—	—	—
	30:42:41.74	786	<4.6	<4.6	<4.6	—	—	—	<3.5	<3.5	<3.5	<6.30e+34
	1.5	2023	16.2(5.7)	9.0 ^b (3.0)	<17.6	—	—	—	6.2(2.2)	<6.8	<13.2	1.10e+35
013453.2+305718	01:34:53.225	1730	—	—	—	—	—	—	—	—	—	—
	30:57:18.28	786	—	—	—	—	—	—	—	—	—	—
	2.0	2023	106.6(12.6)	71.0(10.0)	26.7(6.7)	14.7(5.6)	58.9(9.1)	32.7(8.1)	45(5.3)	30(4.2)	12(2.9)	8.01e+35
013453.8+305744	01:34:53.843	1730	—	—	—	—	—	—	—	—	—	—
	30:57:44.79	786	—	—	—	—	—	—	—	—	—	—
	4.8	2023	13.0 ^b (3.6)	14.4(5.5)	<9.3	—	—	—	9.8 ^b	6.2(2.3)	<7.0	1.75e+35 ^b

Table 3—Continued

Source CXO J	Coord./Unc. RA/Dec/["]	ObsId	Counts						Flux[10^{-7} cts/s/cm 2] ^a			L [erg/s] ^a 0.3–8.0
			0.3–8.0	0.3–2.0	2.0–8.0	0.3–1.0	1.0–2.1	2.1–8.0	0.3–8.0	0.3–2.0	2.0–8.0	
013455.3+304624	01:34:55.304	1730	—	—	—	—	—	—	<5.0	<3.5	<5.0	<9.00e+34 1.95e+35
	30:46:24.21	786	<6.6	<4.6	<6.6	—	—	—	—	—	—	
	1.2	2023	29.5(6.7)	9.6(4.3)	20.3(5.8)	0.5(2.3)	9.5(4.3)	19.3(5.7)	11(2.5)	3.6(1.6)	7.5(2.1)	
013455.9+304814	01:34:55.922	1730	—	—	—	—	—	—	—	—	—	— — —
	30:48:14.77	786	—	—	—	—	—	—	—	—	—	
	1.2	2023	16.4(5.3)	11.7(4.6)	<13.8	—	—	—	6.0(2.0)	4.3(1.7)	<10.4	
013456.1+304138	01:34:56.174	1730	—	—	—	—	—	—	—	—	—	— — —
	30:41:38.10	786	<6.6	<6.6	<4.6	—	—	—	<5.0	<5.0	<3.5	
	2.0	2023	10.8(4.7)	11.9(4.7)	<6.6	—	—	—	4.6(2.0)	4.9(1.9)	<5.0	
013456.7+304556	01:34:56.798	1730	—	—	—	—	—	—	—	—	—	— — —
	30:45:56.01	786	5.9(4.1)	<12.2	<9.7	—	—	—	6.5(4.2)	<9.2	<7.3	
	1.3	2023	<6.0	<6.6	<4.6	—	—	—	<4.5	<5.0	<3.5	
013456.9+304626	01:34:56.966	1730	—	—	—	—	—	—	—	—	—	— — —
	30:46:26.42	786	—	—	—	—	—	—	—	—	—	
	1.3	2023	6.7(3.8)	6.9(3.8)	<4.6	—	—	—	2.5(1.4)	2.6(1.4)	<3.5	
013457.3+304319	01:34:57.344	1730	—	—	—	—	—	—	—	—	—	— — —
	30:43:19.44	786	<8.5	<8.5	<4.6	—	—	—	<6.4	<6.4	<3.5	
	1.6	2023	9.0 ^b (3.0)	8.9(4.3)	<6.6	—	—	—	6.8 ^b	3.4(1.6)	<5.0	
013457.7+304247	01:34:57.763	1730	—	—	—	—	—	—	—	—	—	— — —
	30:42:47.05	786	<4.6	<4.6	<4.6	—	—	—	<3.5	<3.5	<3.5	
	1.8	2023	20.4(6.0)	<6.0	21.7(6.0)	<1.9	0.4(2.3)	20.8(5.9)	8.5(2.5)	<4.5	9.1(2.5)	1.51e+35
013458.5+304707	01:34:58.584	1730	—	—	—	—	—	—	—	—	—	— — —
	30:47:07.27	786	—	—	—	—	—	—	—	—	—	
	1.3	2023	47.7(8.3)	23.8(6.1)	21.3(5.9)	4.2(3.4)	23.2(6.0)	20.0(5.9)	18(3.2)	9.0(2.3)	8.1(2.2)	3.25e+35
013459.2+304608	01:34:59.236	1730	—	—	—	—	—	—	—	—	—	— — —
	30:46:08.02	786	—	—	—	—	—	—	—	—	—	
	1.4	2023	20.5(5.9)	8.7(4.1)	9.1(4.4)	2.5(2.9)	7.5(4.0)	10.2(4.6)	7.6(2.2)	3.2(1.5)	3.4(1.7)	1.36e+35
013500.5+305028	01:35:00.574	1730	—	—	—	—	—	—	—	—	—	— — —
	30:50:28.81	786	—	—	—	—	—	—	—	—	—	
	1.6	2023	82.3(10.5)	44.7(7.9)	37.6(7.5)	3.6(3.4)	44.6(7.8)	33.2(7.2)	31(4.0)	17(3.0)	14(2.9)	5.59e+35
013501.1+304345	01:35:01.127	1730	—	—	—	—	—	—	—	—	—	— — —
	30:43:45.33	786	85.6(12.7)	53.6(9.1)	<33.7	20.3(6.6)	50.7(8.8)	16.9(7.9)	78(11)	47(8.0)	<25.3	1.40e+36
	1.2	2023	180.6(14.9)	120.7(12.1)	51.6(8.6)	33.7(7.1)	94.8(10.9)	51.8(8.8)	71(5.9)	47(4.7)	20(3.4)	1.27e+36
013504.2+304344	01:35:04.228	1730	—	—	—	—	—	—	—	—	—	— — —
	30:43:44.50	786	<8.5	<8.5	<4.6	—	—	—	<6.4	<6.4	<3.5	<1.15e+35 1.09e+35
	2.2	2023	13.4(5.5)	8.0 ^b (2.8)	<14.8	—	—	—	6.1(2.4)	6.0 ^b	<11.1	
013504.8+305034	01:35:04.820	1730	—	—	—	—	—	—	—	—	—	— — —
	30:50:34.15	786	—	—	—	—	—	—	—	—	—	
	2.1	2023	8.0 ^b (2.8)	8.9(4.3)	<5.7	—	—	—	6.0 ^b	3.6(1.7)	<4.3	1.07e+35 ^b
013505.6+305004	01:35:05.685	1730	—	—	—	—	—	—	—	—	—	— — —
	30:50:04.47	786	—	—	—	—	—	—	—	—	—	
	2.2	2023	42.8(8.1)	13.9(5.1)	25.2(6.6)	<1.9	18.9(5.6)	26.2(6.5)	21(3.9)	7.5(2.6)	13(3.2)	3.78e+35
013505.8+305429	01:35:05.889	1730	—	—	—	—	—	—	—	—	—	— — —
	30:54:29.06	786	—	—	—	—	—	—	—	—	—	
	3.8	2023	30.6(9.4)	23.4(6.8)	<27.6	9.9(5.1)	12.1(5.3)	15.3(7.0)	19(4.9)	12(3.3)	<20.7	3.44e+35

Table 3—Continued

Source CXO J	Coord./Unc. RA/Dec/["]	ObsId	Counts						Flux[10^{-7} cts/s/cm 2] ^a			L [erg/s] ^a 0.3–8.0
			0.3–8.0	0.3–2.0	2.0–8.0	0.3–1.0	1.0–2.1	2.1–8.0	0.3–8.0	0.3–2.0	2.0–8.0	
013507.3+305210	01:35:07.333	1730	—	—	—	—	—	—	—	—	—	—
	30:52:10.42	786	—	—	—	—	—	—	—	—	—	—
	2.9	2023	44.1(8.3)	9.0(4.3)	29.3(6.9)	3.4(3.4)	9.4(4.4)	30.7(7.1)	17(3.3)	3.5(1.7)	12(2.8)	3.12e+35
013511.1+304257	01:35:11.170	1730	—	—	—	—	—	—	—	—	—	—
	30:42:57.48	786	—	—	—	—	—	—	—	—	—	—
	3.4	2023	29.3(8.9)	12.4(5.2)	<29.6	<3.2	20.6(6.2)	12.0(6.7)	13(3.7)	5.1(2.1)	<22.2	2.33e+35
013512.7+304514	01:35:12.718	1730	—	—	—	—	—	—	—	—	—	—
	30:45:14.46	786	—	—	—	—	—	—	—	—	—	—
	3.1	2023	22.9(6.7)	14.8(5.7)	9.0 ^b (3.0)	1.4(2.9)	12.4(4.8)	9.4(5.0)	9.6(2.8)	6.0(2.3)	6.8 ^b	1.71e+35
013517.0+304407	01:35:17.030	1730	—	—	—	—	—	—	—	—	—	—
	30:44:07.11	786	—	—	—	—	—	—	—	—	—	—
	4.3	2023	20.6(8.2)	18.6(6.5)	<22.8	1.8(3.8)	12.9(5.3)	6.9(6.1)	8.7(3.3)	7.6(2.6)	<17.1	1.55e+35
013517.5+304446	01:35:17.560	1730	—	—	—	—	—	—	—	—	—	—
	30:44:46.41	786	—	—	—	—	—	—	—	—	—	—
	4.2	2023	80.5(11.6)	29.3(7.0)	54.7(9.3)	4.7(4.3)	26.8(6.7)	49.8(9.3)	33(4.7)	12(2.8)	23(3.9)	5.89e+35
013520.9+304236	01:35:20.996	1730	—	—	—	—	—	—	—	—	—	—
	30:42:36.08	786	—	—	—	—	—	—	—	—	—	—
	5.8	2023	25.4(7.8)	18.0(5.9)	<21.4	6.1(4.1)	12.2(5.0)	11.2(5.7)	14(3.8)	8.9(2.8)	<16.1	2.57e+35

^aFor sources with more than 100 counts, luminosity was computed from spectral fit, otherwise $\Gamma = 2$ and $N_H = 6 \times 10^{20}$ cm $^{-2}$ are assumed.^bMost probable value, for details see Sec. 2.^cThe nucleus; because of pileup, counts and flux are not true values.

Table 4. *Chandra* sources with optical counterparts.

Source CXO J	Unc. "	Counterpart RA Dec	Magnitude/Colors			Remarks	Reference
			V	B-V	U-B		
013253.4+303817	6.1	01:32:53.30 +30:38:21.0	19.33	-0.14	-0.59		[IFM93]
013253.9+303312	8.0	01:32:53.62 +30:33:06.4	19.62	1.51	–	M33d-676	[M98]
013256.3+303558	15.4	01:32:56.10 +30:35:52.0	18.40	-0.10	-1.10	B30	[IFM93]
		01:32:56.50 +30:35:50.0	19.27	-0.31	-0.30		[IFM93]
		01:32:56.33 +30:35:52.4	18.19	-0.09	-0.89	B1Ia/B30	[MAP95]
		01:32:56.71 +30:35:49.5	19.44	-0.16	-1.02	O8-9	[MAP95]
		01:32:57.13 +30:36:05.1	20.24	-0.13	-1.11		[MAP95]
		01:32:56.41 +30:35:49.5	19.26	1.80	–	M33d-1785	[M98]
		01:32:56.47 +30:36:01.1	20.10	1.70	–	M33d-798	[M98]
013315.1+305317	8.1	01:33:15.00 +30:53:22.0	17.80	0.70	-0.90	B100,n	[IFM93]
		01:33:15.30 +30:53:19.0	19.10	0.20	-0.70		[IFM93]
		01:33:14.89 +30:53:24.9	19.61	-0.32	-0.84		[MBH96]
		01:33:15.18 +30:53:18.2	18.45	-0.17	-0.69	Of or WN	[MBH96]
		01:33:15.20 +30:53:25.0	17.8			B99	[HS80]
013327.9+303135	5.9	01:33:27.60 +30:31:37.0	20.83	-0.24	–		[RW93]
		01:33:27.90 +30:31:36.0	20.07	-0.13	–		[RW93]
		01:33:27.90 +30:31:34.0	19.68	-0.12	–		[RW93]
		01:33:27.80 +30:31:32.0	20.63	0.10	–		[RW93]
		01:33:27.90 +30:31:31.0	20.10	-0.22	-1.26		[RW93]
		01:33:27.90 +30:31:29.0	19.63	-0.17	–		[RW93]
013328.7+304746	4.5	01:33:28.80 +30:47:46.0	16.50	0.00	-0.70	B133	[IFM93]
		01:33:28.97 +30:47:44.3	16.69	-0.08	-0.82	B1Ia	[MBH96]
		01:33:28.80 +30:47:46.0	16.73			B2.5Ia	FSZ 113
013333.6+303108	5.5	01:33:33.80 +30:31:14.0	19.12	-0.05	-1.10		[RW93]
		01:33:33.70 +30:31:12.0	20.32	-0.17	-1.07		[RW93]
013334.1+303210	1.9	01:33:34.00 +30:32:12.0	18.70	0.10	-1.30	n?	[IFM93]
		01:33:34.20 +30:32:09.0	18.50	0.10	-1.20	B194	[IFM93]
		01:33:34.20 +30:32:08.0	18.36	0.04	-1.21		[RW93]
		01:33:34.10 +30:32:08.3	20.28	0.21	-0.64		[MAP95]
		01:33:34.12 +30:32:11.0	18.32	-0.06	-0.83		[MBH96]

Table 4—Continued

Source CXO J	Unc. "	Counterpart RA Dec	Magnitude/Colors			Remarks	Reference
			V	B-V	U-B		
013336.0+303333	2.6	01:33:36.00 +30:33:31.0	20.48	-0.12	-0.50		[RW93]
013341.5+303220	3.2	01:33:41.50 +30:32:20.0	16.50	0.81	0.16		[RW93]
	3.2	01:33:41.30 +30:32:19.0	20.36	-0.05	-1.03		[RW93]
	3.2	01:33:41.30 +30:32:19.0	20.41	0.02	–		[RW93]
013358.4+303332	2.3	01:33:58.30 +30:33:33.0	19.52	-0.15	-1.05		[RW93]
013359.0+303425	1.8	01:33:59.20 +30:34:25.0	19.50	0.00	-1.10		[IFM93]
		01:33:59.00 +30:34:26.0	19.56	-0.15	-1.15	assoc. 54	[RW93]
013402.8+304151	1.0	01:34:02.91 +30:41:51.6	18.79	-0.20	-0.87		[MBH96]
013408.3+304633	2.1	01:34:08.20 +30:46:36.0	19.20	0.10	-0.70		[IFM93]
		01:34:08.50 +30:46:35.0	17.00	0.10	-0.90	B401	[IFM93]
013416.3+305154	1.7	01:34:16.30 +30:51:56.0	16.40	0.00	-1.30	M	[IFM93]
		01:34:16.30 +30:51:53.0	17.70	0.10	-1.30	B384,M	[IFM93]
		01:34:16.46 +30:51:54.1	16.22	0.35	-0.72	B384?	[MBH96]
013438.9+305014	22.9	01:34:38.60 +30:50:12.0	19.47	0.00	-0.84		[IFM93]

Note. — [IFM93] Ivanov et al. (1993), [MAP95] Massey et al. (1995), [MBH96] Massey et al. (1996), [RW93] Regan & Wilson (1993), [M98] Massey (1998)

Table 5. *Chandra*-ROSAT matches. ROSAT data from (Haberl & Pietsch 2001).

<i>Chandra</i> source			ROSAT source			
CXO J	Uncert. arcsec	Coordinates RA Dec	Uncert. arcsec	Name	HRI rate [10 ⁻⁴ cts/s]	
013253.4+303817	6.1	01:32:53.400 +30:38:15.00	2.3	R027	20.10 ± 1.90	
013253.9+303312	8.0	01:32:53.800 +30:33:10.00	2.6	R028	9.56 ± 1.30	
013308.3+304802	4.8	01:33:08.700 +30:47:52.00	9.8	R040		
013315.1+305317	8.2	01:33:15.100 +30:53:23.00	2.4	R049	188.00 ± 12.00	
013323.8+303517	3.2	01:33:23.800 +30:35:16.00	4.2	R054	1.56 ± 0.43	
013324.4+304403	1.5	01:33:24.300 +30:44:04.00	2.0	R055	67.00 ± 1.80	
013327.7+304647	3.8	01:33:27.500 +30:46:51.00	5.4	R057	2.01 ± 0.54	
013327.9+303135	6.0	01:33:27.800 +30:31:30.00	6.0	R058	2.22 ± 0.60	
013328.7+304746	4.5	01:33:28.900 +30:47:47.00	3.8	R061	3.94 ± 0.62	
013328.9+304216	1.1	01:33:28.900 +30:42:18.00	2.2	R062	10.00 ± 0.73	
013329.4+304912	2.7	01:33:29.500 +30:49:14.00	3.1	R064	10.10 ± 0.90	
013330.5+303404	2.9	01:33:30.600 +30:34:04.00	4.6	R066	1.23 ± 0.37	
013331.1+303333	1.7	01:33:31.200 +30:33:32.00	2.2	R067	14.80 ± 0.89	
013333.6+303108	5.5	01:33:33.700 +30:31:06.00	4.3	R070	2.81 ± 0.55	
013334.1+303210	2.0	01:33:34.100 +30:32:09.00	2.0	R071	92.20 ± 2.10	
013335.9+303627	1.1	01:33:35.900 +30:36:27.00	2.5	R074	3.84 ± 0.49	
013336.0+303333	2.7	01:33:35.900 +30:33:31.00	4.3	R075	1.52 ± 0.40	
013336.4+303742	1.0	01:33:36.400 +30:37:42.00	3.5	R077	1.32 ± 0.36	
013337.5+304718	1.6	01:33:37.500 +30:47:21.00	4.3	R080	2.30 ± 0.49	
013341.8+303848	1.0	01:33:41.800 +30:38:48.00	2.2	R084	7.75 ± 0.64	
013343.4+304630	1.9	01:33:43.200 +30:46:33.00	2.5	R087	5.88 ± 0.62	
013346.5+303748	0.9	01:33:46.600 +30:37:48.00	2.3	R092	6.20 ± 0.59	
013350.5+303821	1.0	01:33:50.400 +30:38:18.00	3.4	R098	5.40 ± 1.30	
013354.8+303310	1.4	01:33:55.000 +30:33:08.00	2.2	R106	10.70 ± 0.76	
013356.7+303729	0.9	01:33:56.800 +30:37:28.00	2.4	R110	2.64 ± 0.40	
013356.8+303706	1.0	01:33:56.800 +30:37:06.00	3.4	R109	1.14 ± 0.34	
013357.0+303500	1.5	01:33:57.100 +30:35:01.00	4.4	R111	1.07 ± 0.33	
013357.1+305134	5.7	01:33:57.300 +30:51:37.00	5.8	R112	3.26 ± 1.00	
013358.4+303332	2.3	01:33:58.600 +30:33:31.00	3.7	R114	1.47 ± 0.38	

Table 5—Continued

<i>Chandra</i> source			ROSAT source			
CXO J	Uncert. arcsec	Coordinates RA Dec	Uncert. arcsec	Name	HRI rate [10 ⁻⁴ cts/s]	
013358.7+305003	2.1	01:33:58.700 +30:50:09.00	5.3	R115	3.44 ± 0.67	
013401.2+303135	2.0	01:34:01.200 +30:31:36.00	3.0	R120	3.99 ± 0.56	
013401.5+303136	2.0	01:34:01.200 +30:31:36.00	3.0	R120	3.99 ± 0.56	
013402.0+303004	2.8	01:34:02.400 +30:30:08.00	12.4	R122		
013407.9+303555	1.8	01:34:07.900 +30:35:53.00	3.5	R124	1.37 ± 0.35	
013408.3+304633	2.1	01:34:08.500 +30:46:35.00	4.3	R126	2.22 ± 0.51	
013409.8+305044	2.1	01:34:10.300 +30:50:52.00	17.1	R128		
013410.5+303946	1.0	01:34:10.600 +30:39:47.00	2.7	R129	1.70 ± 0.35	
013410.6+304223	1.6	01:34:10.800 +30:42:25.00	2.4	R130	5.22 ± 0.56	
013414.1+305352	2.9	01:34:13.700 +30:53:52.00	17.1	R132		
013416.9+303425	4.2	01:34:17.400 +30:34:22.00	5.0	R137	1.42 ± 0.42	
013425.4+302821	6.9	01:34:25.400 +30:28:14.00	11.9	R143	3.94 ± 1.00	
013426.6+303737	5.0	01:34:26.000 +30:37:35.00	11.5	R145		
013428.1+303246	10.1	01:34:28.400 +30:32:54.00	11.9	R146		
013429.7+305026	0.9	01:34:29.100 +30:50:27.00	12.8	R147	11.8 ± 3.10	
013432.1+305158	1.1	01:34:32.800 +30:51:54.00	31.8	R150		
013436.0+303450	11.7	01:34:36.400 +30:34:48.00	3.9	R154	5.56 ± 0.75	
013438.7+304538	0.9	01:34:38.600 +30:45:28.00	14.6	R156		
013439.8+305143	0.9	01:34:40.100 +30:51:48.00	4.7	R158	3.13 ± 1.10	
013445.0+304927	0.9	01:34:45.200 +30:49:24.00	10.5	R161	5.01 ± 1.10	
013500.9+304346	1.5	01:35:01.300 +30:43:50.00	6.3	R168	5.18 ± 1.80	

Table 6. *Chandra*-XMM matches. XMM-Newton data from (Pietsch et al. 2004).

<i>Chandra</i> source		XMM source			
CXO J	Uncert. arcsec	Coordinates RA Dec		Flux [erg cm ⁻² s ⁻¹]	X-ray ID
013253.4+303817	2.6	1:32:53.46	30:38:14.9	1.32e-13 ± 2.9e-15	X-1,SB1,LCB5,HP27
013253.9+303312	3.0	1:32:53.82	30:33:12.1	1.14e-13 ± 2.8e-15	X-2,SB2,LCB6,HP28
013308.3+304802	2.5	1:33:08.21	30:48:04.3	1.12e-14 ± 1.1e-15	LCB10,HP40
013315.1+305317	0.7	1:33:15.03	30:53:17.9	1.06e-12 ± 1.3e-14	X-4,SB5,LCB13,HP49
013321.7+303858	1.4	1:33:21.66	30:38:58.8	3.85e-15 ± 7.3e-16	
013321.9+303921	1.4	1:33:22.02	30:39:22.3	3.05e-15 ± 7.1e-16	
013323.8+303517	1.6	1:33:23.86	30:35:18.0	6.66e-15 ± 7.7e-16	HP54
013323.9+304821	3.2	1:33:23.79	30:48:20.1	1.03e-14 ± 1.1e-15	
013324.4+304401	0.7	1:33:24.31	30:44:02.8	5.13e-13 ± 6.0e-15	X-5,SB6,LCB15,HP55
013325.5+303618	1.4	1:33:25.47	30:36:17.1	4.43e-15 ± 7.5e-16	
013327.7+304645	1.3	1:33:27.69	30:46:47.4	4.66e-15 ± 6.4e-16	
013327.9+303135	2.3	1:33:27.88	30:31:36.1	2.99e-15 ± 4.0e-16	HP58
013328.7+304746	2.4	1:33:28.78	30:47:44.5	7.48e-15 ± 7.1e-16	HP61
013329.0+304216	1.0	1:33:28.92	30:42:16.9	2.45e-14 ± 9.9e-16	SB8,LCB18,HP62
013329.2+304537	1.6	1:33:29.21	30:45:38.7	5.79e-15 ± 9.7e-16	
013329.2+304508	1.1	1:33:29.19	30:45:09.1	2.14e-14 ± 1.2e-15	SB9,LCB17,HP63
013329.4+304912	1.7	1:33:29.31	30:49:10.7	1.73e-14 ± 1.0e-15	
013330.5+303404	1.5	1:33:30.56	30:34:04.1	1.80e-14 ± 1.2e-15	HP66
013331.1+303333	1.1	1:33:31.19	30:33:33.3	3.88e-14 ± 1.2e-15	X-14,SB11,LCB20,HP67
013333.0+304920	3.0	1:33:32.70	30:49:17.5	5.50e-15 ± 9.9e-16	
013333.6+303108	2.2	1:33:33.70	30:31:10.3	8.22e-15 ± 8.9e-16	HP70
013334.1+303714	1.0	1:33:34.16	30:37:14.8	3.13e-15 ± 6.8e-16	
013334.1+303210	0.7	1:33:34.07	30:32:11.6	6.82e-13 ± 6.2e-15	X-7,SB12,LCB21,HP71
013334.5+303556	1.1	1:33:34.53	30:35:55.0	2.42e-15 ± 4.7e-16	
013335.9+303627	1.0	1:33:35.89	30:36:27.6	1.01e-14 ± 6.4e-16	SB13,LCB22,HP74
013336.0+303333	1.4	1:33:35.86	30:33:31.9	5.31e-15 ± 7.0e-16	HP75
013336.3+303742	1.0	1:33:36.27	30:37:42.0	1.13e-14 ± 9.4e-16	HP77
013337.4+304718	1.2	1:33:37.32	30:47:18.6	1.75e-14 ± 1.3e-15	LCB23,HP80
013339.2+304049	1.0	1:33:39.17	30:40:51.0	4.96e-15 ± 8.0e-16	

Table 6—Continued

<i>Chandra</i> source				XMM source	
CXO J	Uncert. arcsec	Coordinates		Flux [erg cm ⁻² s ⁻¹]	X-ray ID
		RA	Dec		
013340.0+304323	1.0	1:33:40.01	30:43:22.4	4.18e-15 ± 8.0e-16	
013341.5+303220	1.5	1:33:41.54	30:32:19.7	1.39e-14 ± 9.7e-16	
013341.5+304136	1.0	1:33:41.48	30:41:35.2	4.33e-15 ± 6.7e-16	
013341.8+303848	1.0	1:33:41.80	30:38:48.8	1.49e-14 ± 8.6e-16	SB14,LCB24,HP84
013342.5+304253	1.0	1:33:42.36	30:42:53.7	7.05e-15 ± 8.8e-16	HP86
013343.4+304630	1.1	1:33:43.26	30:46:30.7	1.43e-14 ± 9.4e-16	LCB25,HP87
013346.5+303748	1.0	1:33:46.52	30:37:50.0	2.06e-14 ± 1.3e-15	SB15,LCB26,HP92
013351.0+303937	0.7	1:33:50.84	30:39:37.1	1.10e-11 ± 2.8e-14	X-8(nuc),SB16,LCB28,HP102
013354.6+304519	1.1	1:33:54.67	30:45:21.4	2.08e-15 ± 3.6e-16	HP103?
013354.8+303309	1.1	1:33:54.89	30:33:11.4	2.84e-14 ± 1.0e-15	X-13,SB17,LCB29,HP106
013356.8+303729	1.0	1:33:56.75	30:37:30.0	2.33e-14 ± 1.4e-15	LCB30,HP110
013356.8+303706	1.0	1:33:56.77	30:37:08.4	8.74e-15 ± 9.9e-16	HP109
013357.2+305136	3.5	1:33:56.93	30:51:37.1	4.62e-15 ± 8.0e-16	LCB31,HP112
013358.1+303200	1.6	1:33:57.80	30:32:03.5	3.90e-15 ± 7.3e-16	
013358.4+303333	1.3	1:33:58.49	30:33:35.0	4.87e-15 ± 5.1e-16	HP114
013358.8+305004	1.5	1:33:58.70	30:50:04.6	8.76e-15 ± 9.3e-16	LCB32,HP115
013359.0+303425	1.2	1:33:59.24	30:34:26.5	4.23e-15 ± 6.7e-16	
013400.0+303057	2.0	1:34:00.15	30:30:59.1	3.70e-15 ± 7.4e-16	
013400.2+304218	1.0	1:34:00.26	30:42:18.7	3.65e-15 ± 5.6e-16	part of HP121
013402.0+303004	1.4	1:34:02.00	30:30:05.3	3.00e-14 ± 1.4e-15	HP122
013402.6+304939	2.1	1:34:02.75	30:49:41.9	4.20e-15 ± 7.3e-16	
013402.8+304151	1.0	1:34:02.86	30:41:51.7	5.40e-15 ± 8.6e-16	part of HP121
013407.8+303553	1.2	1:34:07.76	30:35:54.5	7.82e-15 ± 7.6e-16	HP124
013408.4+304632	1.5	1:34:08.28	30:46:34.5	5.21e-15 ± 4.8e-16	LCB34,HP126
013409.7+303259	1.8	1:34:09.57	30:32:58.8	2.23e-15 ± 5.9e-16	
013409.9+303219	1.3	1:34:09.99	30:32:20.9	3.14e-15 ± 5.3e-16	
013410.3+305346	2.4	1:34:10.30	30:53:45.3	4.33e-15 ± 7.1e-16	
013410.5+303946	1.0	1:34:10.41	30:39:46.5	2.64e-14 ± 1.4e-15	HP129
013410.6+304223	1.0	1:34:10.61	30:42:25.1	1.41e-14 ± 7.3e-16	LCB35,HP130

Table 6—Continued

<i>Chandra</i> source		<i>XMM</i> source			X-ray ID
CXO J	Uncert. arcsec	Coordinates		Flux [erg cm ⁻² s ⁻¹]	
		RA	Dec		
013412.8+303554	1.4	1:34:12.90	30:35:56.1	3.87e-15 ± 7.0e-16	
013416.3+305154	1.3	1:34:16.51	30:51:55.0	2.46e-15 ± 4.6e-16	HP134?
013416.7+305101	1.2	1:34:16.71	30:51:01.8	4.67e-15 ± 7.3e-16	HP139?
013417.0+303425	1.9	1:34:17.08	30:34:25.8	7.08e-15 ± 8.2e-16	LCB36,HP137
013419.2+304942	1.0	1:34:19.48	30:49:41.1	2.09e-15 ± 5.7e-16	
013421.1+303928	1.6	1:34:20.94	30:39:31.4	1.86e-15 ± 4.9e-16	
013421.2+304932	1.0	1:34:21.13	30:49:32.4	6.14e-15 ± 7.3e-16	
013423.5+305426	1.7	1:34:23.31	30:54:23.8	1.15e-15 ± 5.0e-16	
013423.8+303847	1.9	1:34:23.81	30:38:46.3	8.54e-15 ± 9.2e-16	
013424.5+304306	1.2	1:34:24.55	30:43:07.2	2.19e-15 ± 5.7e-16	
013425.4+302821	2.4	1:34:25.72	30:28:18.0	9.35e-15 ± 9.3e-16	HP143
013426.5+304446	1.0	1:34:26.42	30:44:46.4	5.93e-15 ± 7.1e-16	
013426.6+303737	2.3	1:34:26.58	30:37:40.3	3.34e-15 ± 6.1e-16	LCB37,HP145
013427.0+304314	1.0	1:34:26.93	30:43:14.2	7.47e-15 ± 7.5e-16	
013428.1+303246	3.6	1:34:28.16	30:32:48.0	7.61e-15 ± 8.5e-16	LCB39,HP146
013429.1+304212	1.2	1:34:29.08	30:42:16.0	1.18e-15 ± 4.1e-16	
013429.7+305026	1.0	1:34:29.72	30:50:27.2	6.19e-15 ± 7.3e-16	HP147
013432.0+303455	1.8	1:34:31.99	30:34:53.6	2.02e-14 ± 1.5e-15	
013432.1+305158	1.0	1:34:32.06	30:51:59.7	2.38e-14 ± 1.2e-15	HP150
013432.5+305035	1.0	1:34:32.44	30:50:37.4	3.36e-15 ± 6.7e-16	
013432.7+303436	3.7	1:34:32.44	30:34:37.0	4.91e-15 ± 7.2e-16	
013435.0+304439	1.0	1:34:34.89	30:44:40.2	4.83e-15 ± 7.4e-16	
013435.1+305646	1.5	1:34:35.09	30:56:47.0	2.75e-14 ± 1.7e-15	
013436.0+303450	4.3	1:34:35.92	30:34:50.2	1.08e-14 ± 9.6e-16	LCB41,HP154
013438.8+304538	1.0	1:34:38.67	30:45:40.1	1.66e-14 ± 9.8e-16	HP156
013438.8+305504	0.7	1:34:38.74	30:55:05.2	1.90e-13 ± 3.6e-15	X-9a,LCB42,HP157
013439.8+305143	1.0	1:34:39.87	30:51:44.4	7.83e-15 ± 8.1e-16	HP158
013441.0+304325	1.1	1:34:40.93	30:43:28.5	4.84e-15 ± 4.5e-16	
013442.0+305229	1.1	1:34:41.98	30:52:28.9	4.40e-15 ± 7.5e-16	

Table 6—Continued

CXO J	<i>Chandra</i> source		XMM source		X-ray ID
	Uncert.	Coordinates	RA	Dec	
	arcsec				
013442.5+305249	1.2	1:34:42.41	30:52:49.2	8.22e-15 ± 8.6e-16	
013442.8+304505	1.0	1:34:42.67	30:45:06.7	9.84e-15 ± 8.9e-16	
013444.6+305535	1.3	1:34:44.60	30:55:36.5	2.83e-14 ± 1.6e-15	HP160
013447.4+303958	2.1	1:34:47.30	30:40:01.1	3.62e-15 ± 7.3e-16	
013449.0+304446	1.1	1:34:48.98	30:44:47.9	9.09e-15 ± 8.8e-16	
013449.3+304808	1.0	1:34:49.42	30:48:09.5	1.71e-15 ± 4.0e-16	
013451.1+304356	1.2	1:34:51.04	30:43:58.5	3.43e-15 ± 6.7e-16	
013451.9+304615	1.0	1:34:51.87	30:46:16.8	8.83e-15 ± 9.2e-16	LCB46,HP165
013453.2+305718	2.0	1:34:53.25	30:57:18.2	1.26e-14 ± 1.2e-15	HP163?
013458.5+304707	1.3	1:34:58.42	30:47:08.6	4.11e-15 ± 7.4e-16	
013500.5+305028	1.6	1:35:00.33	30:50:28.9	6.54e-15 ± 9.1e-16	
013505.6+305004	2.1	1:35:05.68	30:50:06.5	8.13e-15 ± 9.2e-16	
013505.8+305429	3.8	1:35:05.84	30:54:28.6	2.79e-15 ± 8.4e-16	
013507.3+305210	2.9	1:35:07.31	30:52:09.8	4.50e-15 ± 8.8e-16	
013512.7+304514	3.1	1:35:12.77	30:45:14.6	2.30e-15 ± 7.4e-16	
013517.5+304446	4.2	1:35:17.74	30:44:46.7	8.61e-15 ± 1.5e-15	